© 2022. Published by The Company of Biologists Ltd | Development (2022) 149, dev200774. doi:10.1242/dev.200774

RESEARCH ARTICLE

A microfluidic platform to investigate the role of mechanical constraints on tissue reorganization

Sham L. Tlili[1,2,*], François Graner[1] and Hélène Delanoë-Ayari[3]

ABSTRACT

Mechanical constraints have a high impact on development processes, and there is a need for new tools to investigate the role of mechanosensitive pathways in tissue reorganization during development. We present here experiments in which embryonic cell aggregates are aspired through constrictions in microfluidic channels, generating highly heterogeneous flows and large cell deformations that can be imaged using two-photon microscopy. This approach provides a way to measure *in situ* local viscoelastic properties of 3D tissues and connect them to intracellular and intercellular events, such as cell shape changes and cell rearrangements. These methods could be applied to organoids to investigate and quantify rheological properties of tissues, and to understand how constraints affect development.

KEY WORDS: Cell aggregates, Tissue rheology, Cell rearrangements, Microfluidics, Microscopy

INTRODUCTION

During embryo morphogenesis or wound healing, biological tissues are sculpted by active processes, such as cell growth and division, cell migration or cell differentiation (Heisenberg and Bellaïche, 2013). These processes generate mechanical stresses within the tissue that can trigger tissue-scale flows, cell deformation and cell rearrangements. The nature of the response of the tissue to mechanical stresses depends on its rheological properties at the scale of a 'cell group' or 'representative volume element' or 'cohort of cells' (Khalilgharibi et al., 2016). In turn, these cell-group-scale properties arise from the cell-scale interplay between cell viscoelasticity and cell-cell interactions, such as adhesion.

To understand fully and measure these properties, 3D *in vitro* tissues, such as cancer cell spheroids or embryonic organoids (Takebe and Wells, 2019), play an increasingly important role in biophysical and medical studies as they are easy to handle and their properties are relevant to further understanding *in vivo* tissues.

To study this *in vitro* tissue rheology in the context of developmental biology, several experimental setups have already been used, including cell monolayers stretching (Harris et al., 2012), rounding of cell aggregates (Mombach et al., 2005; Marmottant et al., 2009; Grosser et al., 2021), shearing of cell monolayers or cell aggregates (Fernández et al., 2007; Stirbat, 2013; Guevorkian et al., 2010; Yousafzai et al., 2020 preprint), and compression of cell aggregates (Marmottant et al., 2009; Montel et al., 2012; Mary et al., 2022). These experiments have enabled bulk parameters, such as shear and compression moduli, viscosity, and yield deformation or yield stress, to be measured. To connect these mechanical properties to cellular processes, it is essential to have access at the same time to the cell structure and to its dynamics (e.g. cell shapes or rearrangements) (Hopkins et al., 2022).

Live imaging *in vivo* (during embryo development or insect metamorphosis, for instance) or *in vitro* provides the opportunity to track cell movements and divisions, cell shape variations and cell rearrangements, and to quantify their contributions to the cell-group or tissue-scale dynamics, by measuring their contributions to the cell-group or tissue deformation rate, for example (Guirao et al., 2015; Etournay et al., 2015).

Methods combining the application of an external stress, force, deformation or deformation rate controlled by the experimentalist with live imaging at subcellular resolution have proven to be powerful approaches to investigate biological tissues and, more generally, the rheological properties of complex materials. For example, cell monolayers can be stretched by being suspended between rods or on an elastic membrane while imaging the tissue response at the cellular level (Wyatt et al., 2015; Fouchard et al., 2020). Nanometric magnetic beads naturally endocytosed by cells have also been used to apply a global force on cell aggregates (Du et al., 2017; Mary et al., 2022).

A fruitful approach for 3D tissues is to embed ferro-magnetic droplets within the tissue, which can be actively deformed by an externally applied magnetic field while imaging the tissue response at the cell scale. This method has enabled the measurement of spatial gradients of yield stress leading to a liquid-solid transition in the zebrafish mesoderm, and also gives access to the visco-elastic response of cells at short time scales (Mongera et al., 2018). This approach provides a powerful method to probe local tissue rheology for small deformations. To measure effective properties for large deformations, pipette aspiration is used broadly on 3D tissues, such as cancer spheroids (Guevorkian et al., 2010), embryos (e.g. mouse, *Xenopus*; David et al., 2014), chicken (Regev et al., 2022) and explants. However, it is not easy to image the tissue microstructure and its dynamic response in such aspiration geometries. Cell-cell rearrangements are of high importance in developmental biology and are rarely observed in experiments in 3D. There was a need to design a system whereby they could be properly quantified in order to understand which biophysical principles govern their dynamics.

Here, we present a method to study cell-group scale mechanical properties in 3D tissues and to relate these properties to cell-scale characteristics, such as cell shape and heterogeneities in cell protein and gene expression. This approach is inspired from studies on non-living amorphous materials (Cheddadi et al., 2011; Golovkova et al., 2020). Our method combines microfluidic aspirations with two-photon imaging of cell shapes at subcellular resolution.

[1]Université Paris Cité, CNRS, Matières et Systèmes Complexes, UMR7057, F-75006 Paris, France. [2]Aix Marseille Univ, CNRS, IBDM, Turing Center for Living Systems, Marseille, France. [3]Univ Lyon, Univ Claude Bernard Lyon 1, CNRS, Institut Lumière Matière, F-69622, Villeurbanne, France.

*Author for correspondence (sham.tlili@univ-amu.fr)

S.L.T., 0000-0001-6018-9923

Handling Editor: Matthias Lutolf
Received 18 March 2022; Accepted 25 August 2022

Development (2022) 149, dev200774. doi:10.1242/dev.200774

It enables the spatiotemporal patterns of deformations generated within the 3D tissue, the visco-elasto-plastic properties of cell groups, and the dynamics of cell rearrangements to be determined and correlated.

Aspiration geometry, i.e. forcing a 3D cell aggregate to flow through a constriction, enables a heterogeneous flow to be applied. As a consequence, each individual experiment provides a self-sufficient data set with a large enough variation range of cell-group deformations and deformation rates. Moreover, this geometry enables the induction of large deformations and the modification of tissue boundary conditions to probe tissue elasto-capillary behavior.

We pre-confine the aggregate and use a capillary with straight sides (rather than a cylindrical pipette). The tissue is physically constrained in the vertical dimension corresponding to the optical axis. This forces it to flow within the plane of observation (Fig. 1, Movie 1). Such quasi-2D flow facilitates imaging of cell shapes and rearrangements.

In principle, the flow could have a 3D structure, namely depend on the direction z, perpendicular to the device plane. This would be the case, for instance, for an aggregate with a core-shell structure, or any heterogeneous tissue. In that case, our set-up would be suitable to perform 3D image analysis, provided the flow was slow enough. We present experiments performed on homogeneous 3D aggregates of cells that do not have core-shell structures (Fig. S1, Movie 2), and we confirm that we can neglect the flow variation along the z direction (Movie 3).

RESULTS

Aspiration and brightfield microscopy

We first focused on cell-group scale aspects of the flow properties. The use of brightfield or phase-contrast microscopy provides valuable information and enables the velocity field and deformation rate to be mapped in the aspired aggregate. The velocity profile inside the channel was consistent with a plug-flow (Fig. 1D, inset)

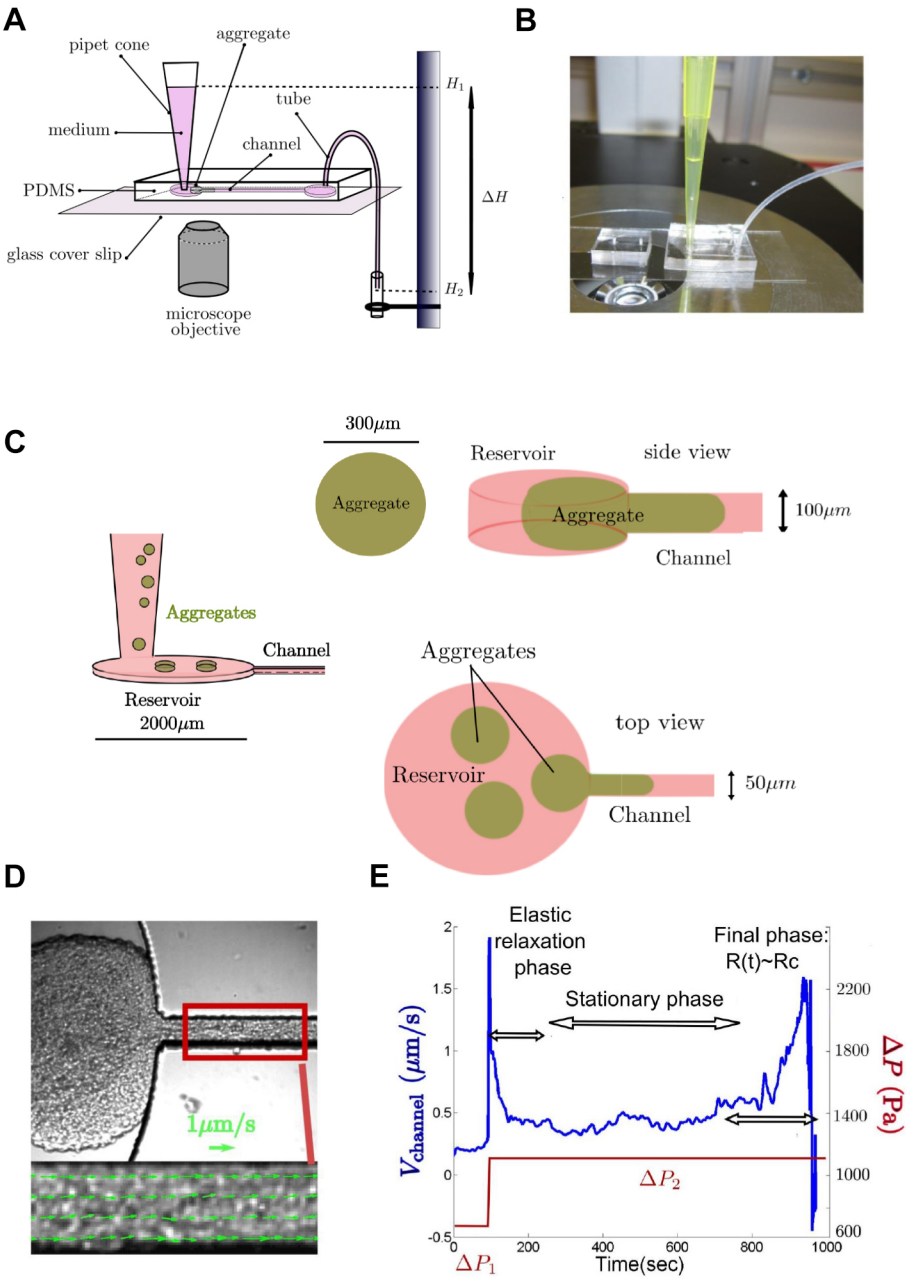

Fig. 1. Aggregate aspiration. (A,B) Schematic and photograph of the microfluidic device used to aspirate aggregates. A hydrostatic pressure difference is applied on the aggregate blocked inside the microfluidic channel. The microfluidic device is on a glass coverslip that allows imaging with an inverted microscope. (C) Microfluidic reservoir and channel top and side views. Preconfinement of the aggregate before aspiration: aggregates are put into the pipet cone, they sediment towards the channel reservoir. A pressure difference is applied inside the channel; the aggregate starts to enter into the reservoir and to deform into a pancake shape. (D) Brightfield image of an aggregate aspired in a channel (Movie 1). The red rectangle indicates the region used to quantify the flow rate. The inset shows the plug flow inside the channel, which we could spatially average to obtain the mean velocity. (E) Aggregate flow rate inside the channel versus time.

Development (2022) 149, dev200774. doi:10.1242/dev.200774

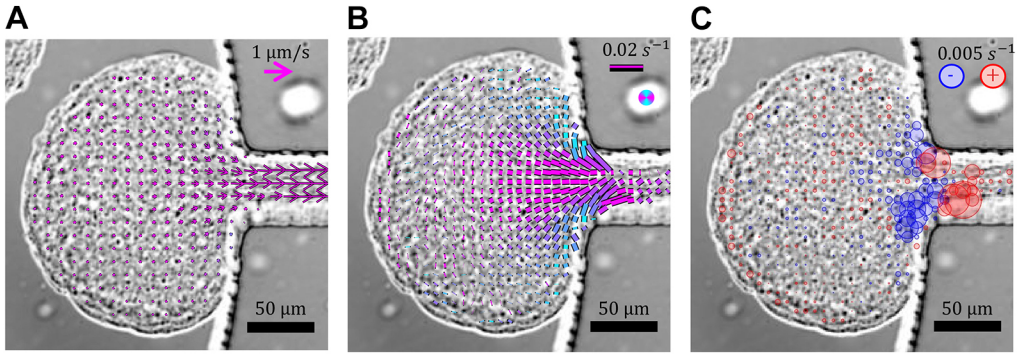

Fig. 2. Aspiration: maps of velocity and deformation, overlaid with brightfield images. (A) Velocity field averaged over 5 min (see scale on top-right corner). (B) Anisotropic part of cell group deformation rate. The direction and length of each bar indicate the local extension rate direction (color-coded) and amplitude (see scale on top-right corner). (C) Isotropic part of cell group deformation rate. The color and size of each circle indicate the local divergence rate sign (red for expansion, blue for compression) and amplitude (see scale on top-right corner).

and we integrated it over the channel cross-section to measure the aggregate flow rate. Over time, we observed three distinct phases of the aspiration (Fig. 1E): (1) a rapid elastic aspiration phase that corresponds to the rapid entrance through elastic cell deformation of the aggregate into the channel; (2) a stationary phase with a fairly constant flow rate, corresponding to an effective viscous behavior of the tissue; and (3) a final phase of acceleration when the non-aspired aggregate part size is similar to the channel size, which indicates that the dissipation on the channel walls is negligible compared with the viscous dissipation inside the aggregate.

Taking advantage of the pseudo-2D flow structure, we quantified the in-plane spatial variation of the flow and deformation rate within the aggregate (Fig. 2A,B). Models (Guevorkian et al., 2010) predict that in a pipette experiment, dissipation occurs only in a typical volume of effective radius R_{channel}. In our setup, we were able to obtain a spatially resolved measurement of the deformation rate: we measured the velocity gradient, symmetrized it to determine the cell-group deformation rate, and plotted its anisotropic part. In our geometry, the typical size of the dissipation zone was similar to R_{channel}, but we observed an extended zone along the walls of the chamber. The isotropic part of the cell group deformation rate (Fig. 2C) revealed compression against the walls before the channel entrance and expansion after the entrance of the channel, which illustrates tissue compressibility.

Cell deformations and rearrangements during aspiration

To investigate the link between the material properties and the cell dynamics, we imaged the tissue at the cell scale to measure cell deformation. Here, we used the same formalism that we used previously on a 2D system (MDCK monolayers; Tlili et al., 2020). Cell divisions can be neglected when they are inhibited, or when the timescale of the experiment T_{exp} is much smaller than the timescale of cell cycle T_{div}; this is the case here, where $T_{\text{exp}} \approx 1$ h and $T_{\text{div}} \approx 12$ h. The cell group (total) deformation rate $\dot{\varepsilon}_{\text{tot}}$ is the sum of the cell deformation rate coarse-grained at the cell-group scale $\dot{\varepsilon}_{\text{cell}}$ and plasticity deformation rate $\dot{\varepsilon}_r$ as a result of the rearrangement rate. The cell deformation pattern is determined by the balance between: (1) the deformation induced by the constriction, i.e. the source term $(\text{grad}\,\vec{v})_{\text{sym}}$; (2) the relaxation of cell deformation due to cell rearrangements ($\dot{\varepsilon}_r$); and (3) the elasticity transport terms (i.e. the fact that non-deformed cells are constantly advected towards the channel). We wanted to estimate the effective viscoelastic relaxation time related to cell rearrangements τ_r (Fig. 3), which can be defined as $\dot{\varepsilon}_{\text{r}} \approx \frac{\varepsilon^{\text{dev}}_{\text{cell}}}{\tau_r}$, where the superscript 'dev' indicates the deviatoric (i.e. anisotropic) part of a tensor.

We imaged at subcellular resolution the process of aspiration and observed simultaneously the heterogeneous velocity and deformation fields (Fig. 4A, Movie 4). To take into account the transport of cell elasticity in the evolution of cell deformation, we measured the spatially averaged cell deformation $\langle\varepsilon^{\text{dev}}_{\text{cell}}\rangle_{\text{box}}$ and the deformation rate $\langle(\text{grad}\,\vec{v})_{\text{sym}}\rangle_{\text{box}}$ in a virtual rectangle advected and deformed by the tissue flow (Fig. 4B) using a home-made code. We can thus evaluate the terms of the evolution equation:

$$\langle\dot{\varepsilon}^{\text{dev}}_{\text{cell}}\rangle_{\text{box}} = \langle(\text{grad}\,\vec{v})^{\text{dev}}_{\text{sym}}\rangle_{\text{box}} - \frac{\langle\varepsilon^{\text{dev}}_{\text{cell}}\rangle_{\text{box}}}{\tau_r}. \quad (1)$$

We can measure at each time point the box-averaged tensors $\langle\varepsilon_{\text{cell}}\rangle_{\text{box}}$ and $\langle(\text{grad}\,\vec{v})_{\text{sym}}\rangle_{\text{box}}$. We also simulated the possible

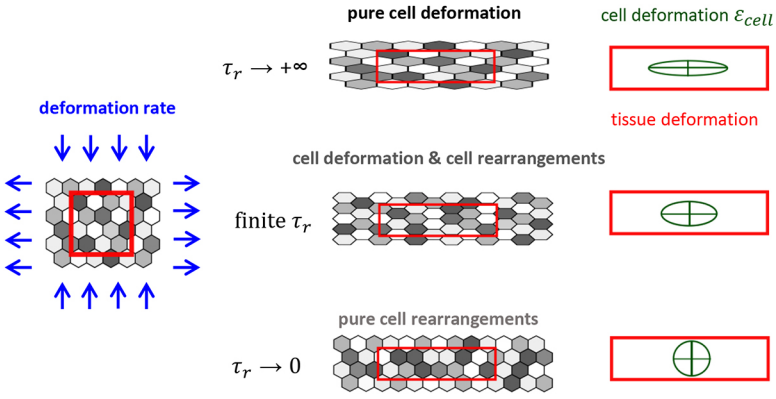

Fig. 3. Effect of deformation rate on cell deformation. The deformation rate is shared between the elastic deformation rate, which results in cell deformation, and the plastic deformation rate, which results in cell rearrangements (Guirao et al., 2015). Their respective shares are determined by the typical timescale τ_r over which the deformation relaxes as a result of rearrangements. In the extreme limit of no rearrangements (top, $\tau_r \to \infty$) cells only deform, and in the opposite limit of instantaneous rearrangements (bottom, $\tau_r \to 0$) cells do not deform at all.

Development (2022) 149, dev200774. doi:10.1242/dev.200774

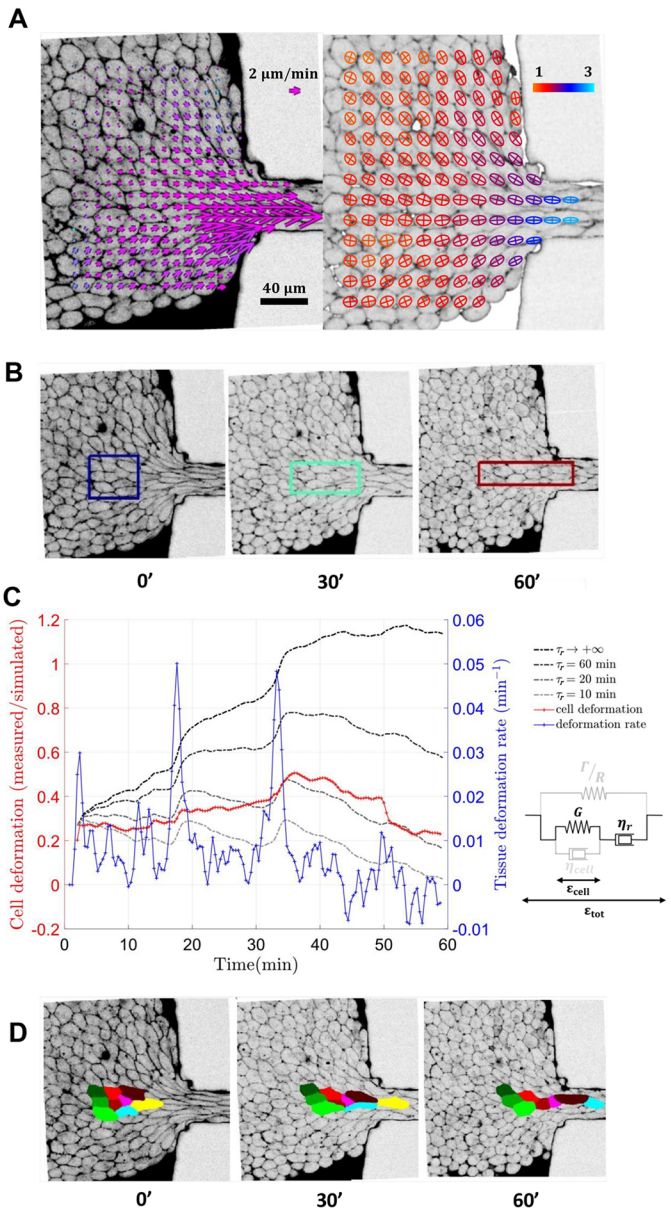

Fig. 4. Quantifying cell shape changes and relaxation during the aspiration. The aggregate is imaged with an inverted two-photon microscope. (A) The optic flow method and Fourier transform method are performed on the cell contours (visible with the sulforhodamine B dye) to measure the velocity field (on the left, averaged over 5 min), and the ellipses representing cell group shape anisotropy (on the right, averaged over 5 min). Anisotropy is color-coded from 1 (red) to 3 (blue). (B) Virtual patch of tissue advected and deformed by the velocity field and its gradient, measured by optic flow (Lagrangian approach). This patch is used to spatially average the tensors in the following analysis. (C) Estimation of the relaxation time τ_r. In blue, anisotropic component of the cell-group deformation rate $\dot{\varepsilon}_{tot}^{xx-yy}$, in red anisotropic component of the cell deformation $\varepsilon_{cell}^{xx-yy}$, in gray levels simulated $\varepsilon_{cell}^{xx-yy}$ for different typical values of the cell shape relaxation timescale τ_r, in black simulated $\varepsilon_{cell}^{xx-yy}$ if there was no cell shape relaxation (purely elastic deformation, $\tau_r \to \infty$). Inset shows rheological model extracted from Fig. 8. (D) Tracking of a cell group in the virtual patch and identification of cell rearrangements. Times are indicated in minutes.

evolutions of $\langle \varepsilon_{cell} \rangle_{box}$ by inserting into Eqn 1 the experimental value of $(\text{grad}\ \vec{v})_{sym}$ and by varying the parameter τ_r (Fig. S3).

In Fig. 4C, we compared the experimental measurement of deformation evolution, $\langle \varepsilon_{cell} \rangle_{box}$ (red curve), with various simulations: we varied τ_r between 10 min (light gray) and infinity (black), the latter being a purely elastic limit (Fig. S3). The simulated deformation amplitude agreed reasonably with the experiment when we used $\tau_r \approx 20$ min. The Fourier determination of deformation was sufficiently discriminant and reproducible to determine correctly the amplitude order of magnitude and we could reasonably exclude values of τ_r outside of the interval [15 min, 25 min] (Fig. S4).

Thus, measurements coarse-grained at the cell-group scale yielded an estimate of an effective cell deformation relaxation time. Because divisions play a negligible role on the experiment timescale, the effective cell deformation relaxation time is necessarily associated with the dynamics of cell rearrangements, which were numerous in particular near the constriction entrance (Fig. S4D, Fig. S5, Movie 5).

This relaxation time value was of same order of magnitude as the one we found for MDCK cells in a 2D migration experiment of cells around an obstacle: $\tau \approx 70$ min (Tlili et al., 2020). Assuming that the effective viscosity at cell-group scale due to rearrangements is:

$$\eta_r \approx G\tau_r, \quad (2)$$

and taking $\eta_r \approx 10^5$ Pa.s as we found previously (Marmottant et al., 2009; Stirbat, 2013), Eqn 2 yields $G \approx 100$ Pa. Given that G is not expected to vary with scale, its value is the same at cell scale and at cell-group scale. It is also expected to be close to the modulus of an isolated cell outside of an aggregate. In fact, the isolated F9 cell modulus is also 100 Pa (Perez et al., 2021).

Note that the determination of τ_r in Fig. 4C is not sensitive to the shape of the deformation evolution. The peaks in deformation are not systematically observed and their origin is unknown; they are likely due to a stick-slip friction on the glass coverslip (rather than to cascades of rearrangements, which we did not detect). Determining accurately the shape of the deformation evolution is beyond the scope of the present study. It would require the time resolution and signal-to-noise ratio to be improved simultaneously beyond the possibilities of the current Fourier method with our current image quality. This would be possible in principle using cell contour segmentation complemented with detailed tensorial analysis.

Cell rearrangement dynamics

Using the same data, but at cell scale, we have access to the cell rearrangements dynamics at the scale of a single event (Fig. 5A) by manually identifying and segmenting cell-cell contacts that are disappearing and newly created.

As the deformation rate and cell deformation fields are heterogeneous, we can trigger in the same experiment: (1) 'quasi-static' rearrangements in deformed regions of the tissue away from the channel, where both a disappearing link between cells losing contact and a newly appearing link between cells gaining a new contact can be clearly identified; and (2) 'sliding' rearrangements at the vicinity of the channel, where cells are highly stretched, flow rapidly and seem to slide across each other. In the first case, where rearrangements can be clearly identified and well-defined, we manually measured the disappearing and appearing junction lengths versus time (Fig. 5B). We defined velocities of appearance and disappearance before and after the rearrangement by taking the tangent of the junction length curves before and after the four-fold vertex stage. To establish a robust definition, we defined the velocity of disappearance $V^- = L^-(t = -T)/T$ and of creation $V^+ = L^+(t = +T)/T$ at $T = 6$ min. Their values were unchanged at $T = 10$ min, as the length evolution is locally linear around the four-fold vertex stage. We often observed an asymmetry in V^+ and V^- (Fig. 5C).

Development (2022) 149, dev200774. doi:10.1242/dev.200774

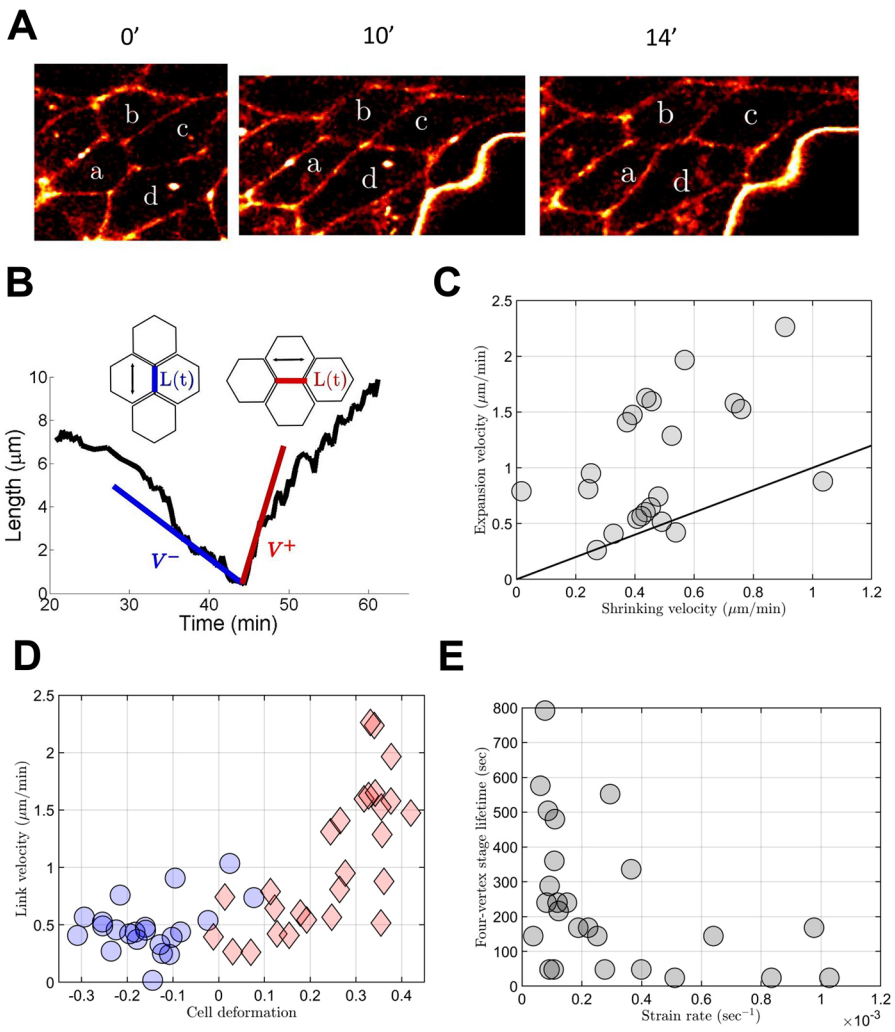

Fig. 5. Cell rearrangements. (A) Typical cell rearrangement in the aspired aggregate. Before the rearrangement, cells a and c are in contact; this contact progressively disappeared until reaching the four-fold vertex stage. After the rearrangement, a new contact between cells b and d is created. Times are indicated in minutes. (B) Junction length evolution during a rearrangement. Length of the disappearing junction (in blue) and of the newly created one (in red) versus time; see inset for definitions. (C) Asymmetry in junction length evolution speed before and after the four-fold vertex: velocities of creation versus disappearance. (D) Link shrinkage and growth versus deformation: V^- versus ε^-_{cell} (blue) and V^+ versus ε^+_{cell} (red); see text for definitions. (E) Stability of four-fold vertex: time T_{vertex}, during which the junction that undergoes a rearrangement is below a cutoff length L_{small} = 1.5 µm, versus $\dot{\varepsilon}_{tot}$.

To relate these quantities with the local cell deformation during the rearrangement, we projected the tensor ε_{cell} in the direction of the junction that disappeared/appeared, yielding $\varepsilon^-_{cell} = \varepsilon_{cell}\cos(2\theta^-)$ where θ^- is the angle between the disappearing link and the principal direction (i.e. the eigenvector corresponding to the positive eigenvalue) of ε_{cell}; and $\varepsilon^+_{cell} = \varepsilon_{cell}\cos(2\theta^+)$ where θ^+ is the angle between the appearing link and the principal direction of ε_{cell} (Fig. 5D). We observed that the disappearing junction is compressed, and that the newly created junction is elongated, which is consistent with the fact that observed rearrangements are triggered by the cell-group-scale flow imposed by the aspiration.

We plotted V^+ and V^- versus ε^+_{cell} and ε^-_{cell}, which were averaged at the same time, $T = 6$ min, as the velocities in Fig. 5D. For $-0.3 < \varepsilon_{cell} < 0.3$, the velocities V^- and V^+ were around the mean value $\approx$ 0.5 µm/min. For $\varepsilon^+_{cell} > 0.3$, the mean value of V^+ increased suddenly up to $\approx$ 2.5 µm/min (see also Movie 5). Examples of such highly deformed rearranging cells are shown in Figs S4D and 5A; these occurred mainly near the constriction entrance. They were usually compatible with the tissue confluence and integrity. High aspiration pressures and velocity sometimes resulted in aggregate fractures (Movie 6): we did not analyze these experiments.

We also looked at the lifetime T_{vertex} of a 'four-fold vertex stage' (Fig. 5E). We defined it as the stage when the cell-cell junction was below 1.5 µm, which is small compared with the cell size, and large enough to avoid artefacts due to the resolution of the length determination when the junction is small. We observed that the lifetime of a four-fold vertex at null deformation rate can be large, which is qualitatively different from the physics of liquid foams, in which the four-fold vertex is unstable (Cantat et al., 2013). The lifetime of the four-fold vertex in a biological tissue can be related to the dynamics of adhesion remodeling (Bardet et al., 2013; Guirao and Bellaïche, 2017), i.e. the timescale necessary for non-contacting cells to create a new junction. At a high cell deformation but null deformation rate, we could imagine that the four-fold vertex lifetime is dominated by active fluctuations and adhesion remodeling. Conversely, at both high cell deformation and deformation rate, a new contact between cells can be created without maturing cell-cell adhesion (i.e. new contacts and sliding of cells are triggered by the deformation rate).

Aggregate relaxation after aspiration

The aspired aggregate can either relax in a reservoir at the end of the channel or be pushed back into the entrance reservoir. In both cases, the relaxation remains an actual 2D relaxation as the tissue is still confined in the z direction. The relaxation dynamics qualitatively depend on the time the tissue has spent in the channel, and two relaxation regimes can be distinguished.

During a rapid aspiration, there was not enough time for cell rearrangements to occur and the aggregate deformation was due only to cell deformation. In this case, the aggregate shape relaxation in a reservoir corresponded to a cell deformation relaxation on a timescale of minutes (Fig. 6, Movie 7). This corresponds to an

Development (2022) 149, dev200774. doi:10.1242/dev.200774

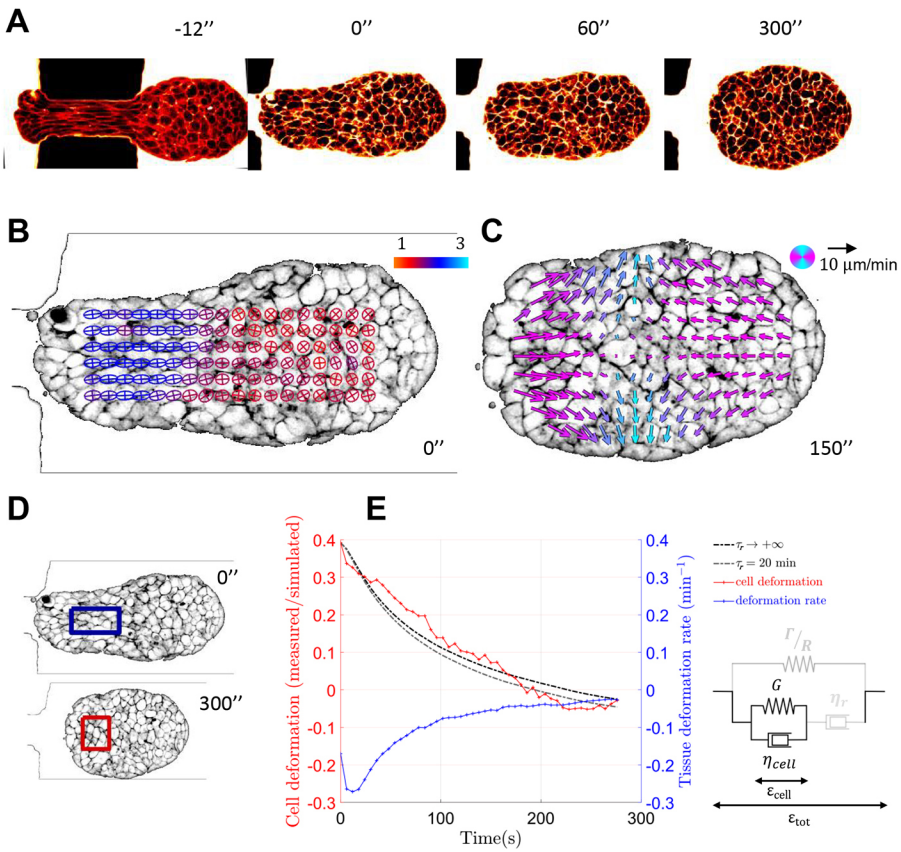

Fig. 6. Aggregate rapid relaxation (same analysis and imaging methods as in Fig. 4). (A) Typical aggregate during the rapid relaxation phase (Movie 7). The aggregate is aspired in a short channel, the right part has time to slowly relax during the aspiration. When the radius of the remaining part of the aggregate to be aspired is of the same size as the channel size (t = – 12 s), the aggregate part still aspired within the channel relaxes quickly (t = 0 s) until the aggregate reaches a symmetrical shape ($t \approx 200$ s). (B) Ellipses representing cell group anisotropy, color-coded from 1 (red) to 3 (blue). (C) Velocity field during the relaxation. (D) Virtual patch of tissue advected and deformed by the velocity field and its gradient, measured by optic flow. (E) In blue, anisotropic component of cell-group deformation rate $\dot{\varepsilon}_{\mathrm{tot}}^{xx-yy}$, in red cell deformation $\varepsilon_{\mathrm{cell}}^{xx-yy}$, in gray levels simulated $\varepsilon_{\mathrm{cell}}^{xx-yy}$ for different typical values of cell shape relaxation timescale τ_r, in black simulated $\varepsilon_{\mathrm{cell}}^{xx-yy}$ if there was no cell shape relaxation (purely elastic deformation, $\tau_r \to \infty$). Times are indicated in seconds. Inset shows rheological model extracted from Fig. 8.

effective visco-elastic solid behavior (Kelvin–Voigt) with a typical timescale of relaxation:

$$\tau_{\mathrm{cell}} \approx \frac{\eta_{\mathrm{cell}}}{G} \approx 100 \text{ s}. \quad (3)$$

Taking $G \sim 100$ Pa, Eqn 3 yields: $\eta_{\mathrm{cell}} \sim 10^4$ Pa.s.

When the aggregate was aspired quasi-statically at a very slow pace ($T_{\mathrm{aspi}} > \tau_r$, as is the case in Fig. 4), the cell deformation had enough time to relax through rearrangements (Fig. 7). In this case, when the aggregate started to relax in the reservoir, the cell shape was already isotropic, but we still observed a relaxation of the aggregate shape (Fig. 7A, Movie 8) associated with an elongation of cells along the axis perpendicular to the aggregate main elongation axis. This phenomenon can be explained by the fact that aggregate surface tension triggers a compaction of the aggregate along its main axis of elongation. Because cells can rearrange and relax their shape under stress on timescales of $\tau_r \sim 20$ min, the aggregate surface tension related compression triggers significant cell deformations without any rearrangement on timescales shorter than τ_r. This is the signature of an elasto-capillary behavior for the tissue, which can happen when the aggregate surface tension Γ is high enough to trigger significant cell deformations. We assume here that the aspiration does not modify the order of magnitude of Γ, which is $\Gamma = 5$ mN/m according to our previous aggregate scale experiments using F9 cells (Stirbat et al., 2013). The typical aggregate curvature radius R at the end of the rounding phase is of order of $R_{\mathrm{channel}}/2 \sim 50$ µm. We thereby obtain:

$$\frac{\Gamma}{R} \approx 100 \text{ Pa}. \quad (4)$$

This value is of same order of magnitude than the elastic modulus G, which confirms that the capillarity is sufficiently large to induce high elastic deformations within the bulk of the aggregate. Fig. S6 shows an example of an aggregate relaxing after being partially aspired sufficiently slowly in a longer channel (Movie 9). After the fast cell shape relaxation, the aggregate did not entirely return to its initial round shape. The aggregate then rounded up as a result of capillarity, and cells re-deformed, within a few minutes (Movies 10, 11). Myosin is essential in this shape relaxation process as when blebbistatin was added, the relaxation was partial: the first fast relaxation was conserved, but not the second slow one (Fig. S7, Movie 12).

In turn, this new elastic deformation can eventually fully relax. This occurs at low shear rate, and long timescales, where cell divisions may also play a role.

To recapitulate the different behaviors observed in the previous sections, we propose a multi-scale rheological diagram of the aggregate (Fig. 8, Table 1). It combines the contributions of intra-cellular rheology (cell deformations), inter-cellular rheology (cell rearrangements) and aggregate surface tension (elasto-capillarity). This complete rheological model could, in principle, apply to all experiments presented here (Figs 4C, 6E and 7E). Ideally, all of them could be fitted with a single set of parameters, at least if elastic and viscous moduli are supposed constant. We, however, emphasize that only the aspiration part of the experiment is here submitted to a quantitative test. The relaxation part could be tested more quantitatively through a finite element simulation taking into account the geometry details.

DISCUSSION

Our experimental set-up uses a microfluidic constriction to impose a highly heterogeneous flow to a 3D cell aggregate, by controlling both the force applied to the aggregate and the flow geometry. It

Development (2022) 149, dev200774. doi:10.1242/dev.200774

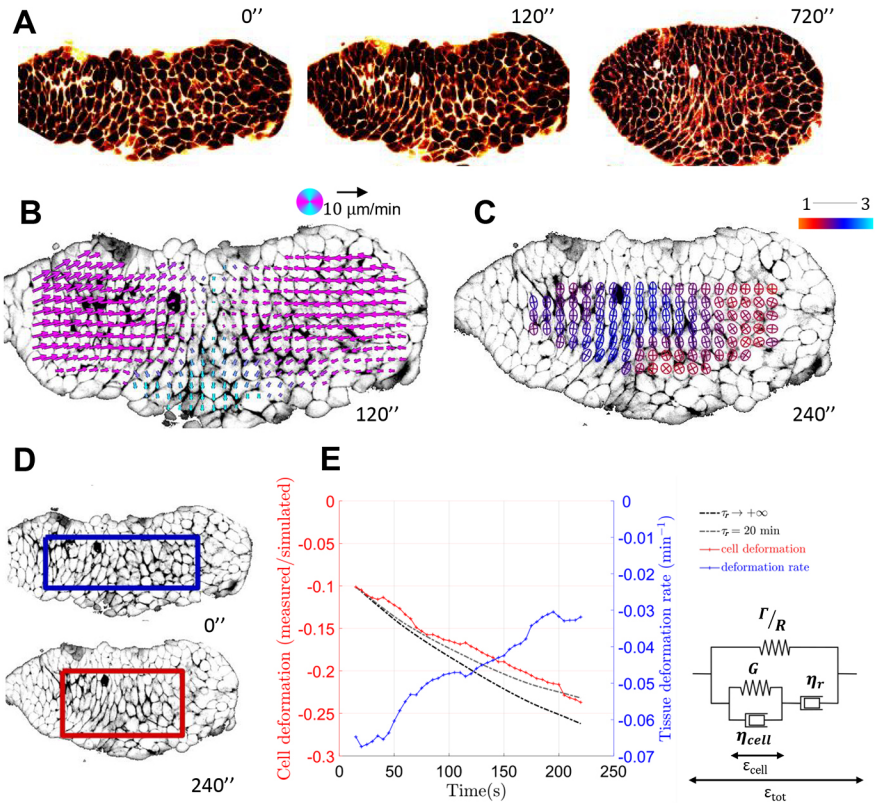

Fig. 7. Aggregate long-term relaxation (same analysis and imaging methods as in Fig. 4). (A) Typical aggregate during the long-term relaxation phase (Movie 8). The aggregate is aspired in a long channel. When the aggregate is released from the channel after a longer time spent in the channel (30 min), it undergoes first a rapid and partial shape relaxation similar to that shown in Fig. 6, associated with cell elongation relaxation along the *x*-axis, and then continues to relax by compressing the cells along the *x*-axis. (B) Velocity field corresponding to the compaction of the aggregate obtained with optic flow. (C) Ellipses representing cell group shape anisotropy color-coded from 1 (red) to 3 (blue). (D) Virtual patch of tissue advected and deformed by the velocity field and its gradient, measured by optic flow. (E) In blue, anisotropic component of cell group deformation rate $\dot{\varepsilon}_{\mathrm{tot}}^{xx-yy}$, in red cell deformation $\varepsilon_{\mathrm{cell}}^{xx-yy}$, in gray levels simulated $\varepsilon_{\mathrm{cell}}^{xx-yy}$ for different typical values of cell shape relaxation timescale τ_r, in black simulated $\varepsilon_{\mathrm{cell}}^{xx-yy}$ if there was no cell shape relaxation (purely elastic deformation, $\tau_r \to \infty$). Times are indicated in seconds. Inset shows rheological model extracted from Fig. 8.

triggers (1) cell deformations, (2) cell rearrangements and (3) global aggregate geometry changes, and enables the interplay between the three to be studied. Using two-photon microscopy, we simultaneously image cell contours at subcellular resolution and quantify mechanical response at the scales of cell, cell group and whole aggregate.

Although the basic principle is similar to micropipette aggregate aspiration, the present set-up has at least three advantages. First, we can study separately, and in detail, the effect of cell group elasticity, aggregate surface tension, and coupling between both (so-called 'elasto-capillarity'). Second, we can reach higher cell deformation, or more precisely we obtain a large product of deformation rate by relaxation time (the so-called 'Weissenberg number', here of order of one); this is probably relevant in fast morphogenetic changes phases such as gastrulation, whereby tissues encounter both high cell deformations and cell deformation rates. Third, we can map different scales and local differences in mechanical properties; we are thus not restricted to homogeneous aggregates.

Perspectives for biophysics

3D cell aggregates are model systems of active fluctuating cellular materials. We propose here to measure tissue-scale effective rheological parameters averaged over time and space. Improvements could include changes in constriction walls, which could be rounded or at angles smaller than 90°. Embedding deformable stress sensors inside the tissue (Mongera et al., 2018; Campàs et al., 2014; Dolega et al., 2017; Souchaud et al., 2022) would enable cell deformation to be determined in relation to the local tissue stress to validate further rheological models; beyond the linear models we test here, future work might investigate more realistic power-law rheologies.

Further progress could come from improved time and space resolution, segmentation and tracking, to obtain better statistics; dynamic stress inference (which applies even to moving junctions) (Brodland et al., 2010; Roffay et al., 2021) could infer junction tensions and determine how they are modulated by cell deformations and rearrangements.

How cell membrane trafficking, adhesion proteins and molecular motors dynamics affect rearrangement dynamics and are relocalized during junction remodeling in 3D tissues is still not well understood (Iyer et al., 2019; Nishizawa et al., 2022 preprint). Combining our method with cell lines endowed with fluorescent reporters of such proteins would enable quantification of their dynamics using fluorescence recovery after photobleaching techniques, for example. Other exciting insights could come from blocking the action of some proteins (using knockout cell lines or chemical inhibition of various pathways and effector proteins) in order to quantify the relative contributions of various components of the cellular machinery to tissue mechanics. Studying the effects of drugs such as blebbistatin, which inhibits myosin II, could also bring new interesting pieces of information, as shown by our proof-of-concept experiments (Fig. S7B, Movie 12). In the same way, cell-cell stress propagation can also be modified for instance using an α-catenin-null cell line. Because α-catenin links the cytoskeleton with cadherins, cell-cell junctions are modified. Aggregates still form cadherin-cadherin junctions, but cell shapes are more irregular, there is a shorter correlation range in both shape and velocity, and rearrangements are dramatically impeded (Movie 13).

Perspectives for developmental biology, spheroids and organoids

Cell rearrangement dynamics have been studied in *in vivo* systems, such as *Drosophila* (Guirao et al., 2015; Etournay et al., 2015; Bardet et al., 2013; Guirao and Bellaïche, 2017; Rauzi et al., 2008) or *Xenopus* embryos (David et al., 2014), *in vitro* tissues (Tlili et al., 2020) and numerically for *in silico* tissues (Bi et al., 2014).

Development (2022) 149, dev200774. doi:10.1242/dev.200774

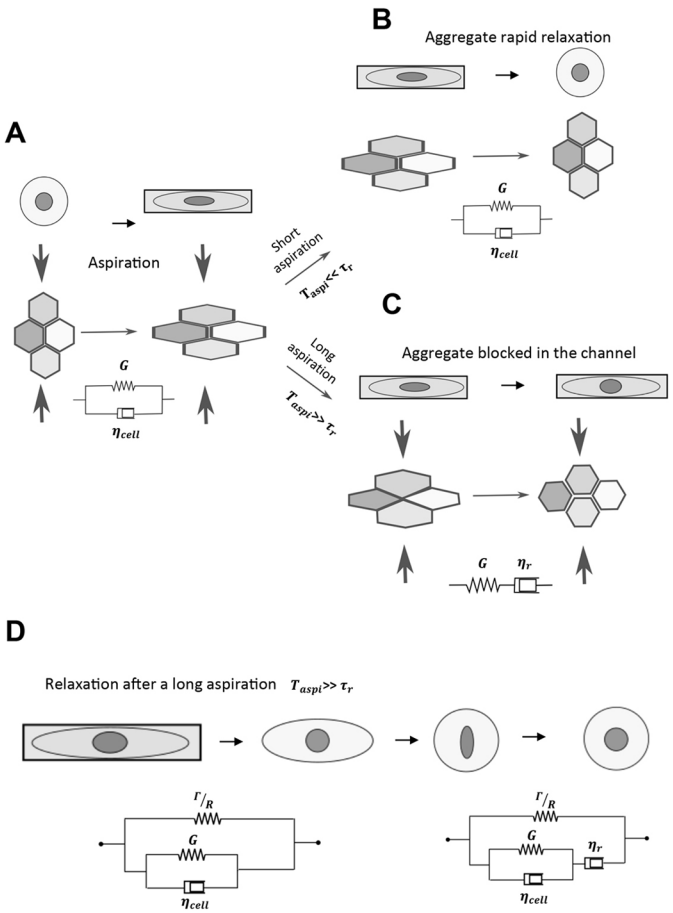

Fig. 8. Proposed rheological diagram for the aggregate. (A) Cell group without rearrangements: cells can be described as a visco-elastic solid (Kelvin–Voigt) with a typical timescale of cell shape relaxation τ_{cell}. (B,C) Schematic representation of what happens during an aspiration and in relaxation experiments depending whether the cell shape has time to relax due to cell rearrangements during the aspiration phase: T_{aspi} either smaller (B) or larger (C) than the relaxation time τ_r. In C, the tissue can be at first order described as a visco-elastic liquid (Maxwell) with a relaxation time τ_r. (D) Schematic rheological diagram proposed for the whole aggregate, with Γ/R an aggregate scale effective capillary modulus as the surface tension drives the aggregate's rounding, until eventually the whole elastic deformation fully relaxes at long timescales. See Table 1 for parameter names and orders of magnitude.

However, in the context of embryo development or collective cell migration *in vitro*, it is difficult to distinguish the rearrangements that build or relax deformation (or stress) (Guirao and Bellaïche, 2017), i.e. those for which cells act as motors, versus those for which cells resist a force imposed from outside. Here, we present an experimental platform suitable for quantitative characterization of the resistant cell rearrangements triggered by an imposed flow.

This microfluidic platform could also be a useful, simple tool for perturbing mechanosensitive pathways by applying shear stresses and to quantify their effect on biomechanical networks (using fluorescent reporters or doing RNA sequencing afterwards, as it is easy to collect the aspired aggregates after the experiment). For this kind of application, the measurement reproducibility (Fig. S4, Movies 14 and 15) enables development of parallel and/or sequential constriction set-ups, as has already been done for single-cell experiments (Brückner et al., 2019).

It has been recently shown that gradients of expression of cadherins are associated with embryonic organoid symmetry breaking and elongation (Hashmi et al., 2022). Whether these gradients are associated with gradients in rheological properties remains unknown in such systems. An advantage of our method is that it relies on the observation and extraction of local mechanical responses in 3D: it could be used to identify spatial heterogeneities in cell-group mechanical responses in systems such as embryonic organoids and correlate them with local protein or gene expression.

This set-up will be very useful for understanding the mechanisms at stake in the response of 3D tissues to mechanical stresses and in particular to obtain new insights into the biophysics of cell-cell rearrangement, which plays a central role in development. We envisage that it could be used in many different systems, such as *Hydra* (from which aggregates can easily be formed), mouse embryos, organoids, and 3D bulk tissues of *Xenopus*, and could yield new information on key developmental processes.

MATERIALS AND METHODS

Manipulation

For these experiments, we used a mouse embryonic carcinoma F9 cell line (Nagafuchi et al., 1987) (American Type Culture Collection, CRL-1720). Aggregates were obtained by resuspending single cells after trypsinization in a dish and preventing them from settling down using an orbital shaker. After 2 days, we obtained aggregates with a diameter around 250 µm.

The experiment was performed on a microfluidic chip (Fig. 1A-C). The PDMS mold was obtained using standard lithography techniques. For the experiments presented here, the channel width was 50 µm and its height 100 µm. After bonding the PDMS chip to a glass coverslip for 60 s using a Plasma Harrick Plasma cleaner on both glass and PDMS, the channel was incubated for 30 min with a 1% Pluronic F-127 solution (Sigma-Aldrich) in order to avoid adhesion of the aggregate to the wall while flowing. It was then rinsed with Leibovitz's L-15 Medium without Phenol Red (Gibco) complemented with 10% fetal bovine serum, which was further used for the experiment. For the introduction of the aggregate, we used a 200 µl cone, and the outlet was then linked to a fluid reservoir the height of which could be adjusted in order to generate a difference in pressure controlled by the difference in height between the sample and the reservoir.

The aggregate was first dropped into a cone pipette. Then, it was sedimented into a 100-µm-high reservoir and deformed into a pancake shape (Fig. 1A-C). After waiting at least 10 min for stress relaxation, the aggregate was pushed towards the channel entrance. Because of the applied pressure

Table 1. Characteristic quantities for the proposed rheological model, and their approximate order of magnitude

Quantity	Symbol	Value	Source
Cell-group scale visco-elastic relaxation time	τ_r	10^3 s	Fig. 4C
Cell-group scale viscosity	η_r	10^5 Pa.s	Marmottant et al., 2009; Stirbat, 2013
Elastic modulus	G	10^2 Pa	Eqn 2
Cell scale visco-elastic relaxation time	τ_{cell}	10^2 s	Figs S6E and 7E
Cell scale viscosity	η_{cell}	10^4 Pa.s	Eqn 3
Aggregate scale capillary modulus	Γ/R	10^2 Pa	Eqn 4

Development (2022) 149, dev200774. doi:10.1242/dev.200774

difference, the aggregate slid into the reservoir towards the channel entrance and started to deform inside the channel (Fig. 1D).

The aggregates were imaged on a two-photon inverted microscope using an oil immersion 40× objective (HCX PL APO CS 40.0×1.25 OIL UV) equipped with MaiTai Spectra Physics laser (690-1060 nm) used at 800 nm, and a lowpass filter below 600 nm, under a temperature control environment set-up at 37°C. To visualize the cell contours, we used a solution of sulforhodamine B (Marmottant et al., 2009). We diluted 16 µl of a stock solution (1 mg/ml) in 1 ml of Leibovitz complete medium. With this method, bleaching is very low as the fluorophore rapidly diffuses from the medium to the extracellular space.

Image analysis

We measured the two-dimensional velocity field $\vec{v}(x,y,t)$ using a custom-made MATLAB optic flow code based on the Kanade–Lucas–Tomasi (KLT) algorithm (Lucas and Kanade, 1981) with a level 2 pyramid. This coarse-grained velocity field can be averaged in time, yielding components $v_i(x_j)$ where $i,j=1$ or 2. Using finite differences, we obtained in each box the deformation rate as the symmetric part of the velocity gradient, $(\mathrm{grad}\,\vec{v})_{\mathrm{sym}}$, with components $(\partial_i v_j+\partial_j v_i)/2$. This symmetric tensor can be diagonalized; we graphically represent in each box the tensors by bars, the direction and length of which correspond respectively to eigenvectors and eigenvalues, with blue bars for compression and red bars for elongation (Fig. S2).

To extract the coarse-grained cell anisotropy, we used Fourier transform (for details and validation, see Durande et al., 2019). In short, the Fourier transform of an image of a connective tissue estimates the cell size, shape and anisotropy averaged over a cell group. This method provides an efficient measurement of the deformation coarse-grained at cell-group scale, without having to recognize and segment each individual cell contour. We used the same grid and box size as for the velocity (box of 256 pixels, overlap 0.75). To improve the signal-to-noise ratio, the Fourier transform norm was smoothed in time by using a sliding average over three consecutive time points.

We defined the cell shape deformation tensor $\varepsilon_{\mathrm{cell}}$ with respect to a rest state which we assumed to be isotropic, with two equal eigenvalues $L_0=(L_{\max}L_{\min})^{1/2}$. Hence, $\varepsilon_{\mathrm{cell}}$ has the same eigenvectors as the Fourier pattern, and two eigenvalues: $\frac{1}{2}(L_{\max}^2/L_0^2-1)$ and $\frac{1}{2}(L_{\min}^2/L_0^2-1)$. The deformation tensor $\varepsilon_{\mathrm{cell}}$ is equivalent to other definitions of the deformation (Graner et al., 2008; Durande et al., 2019) within a linear approximation; in addition, $\varepsilon_{\mathrm{cell}}$ has the advantage of having well-established transport equations (Tlili et al., 2015).

We represent the deviator $\varepsilon_{\mathrm{cell}}^{\mathrm{dev}}=\varepsilon_{\mathrm{cell}}-\mathrm{Tr}(\varepsilon_{\mathrm{cell}})I/2$, where I is the identity tensor; $\varepsilon_{\mathrm{cell}}^{\mathrm{dev}}$ is the anisotropic part of $\varepsilon_{\mathrm{cell}}$ and only depends on the ratio $\frac{L_{\max}}{L_{\min}}$, which is represented by ellipses the color of which indicates the value of the deformation.

Acknowledgements

We thank the Nanoptec platform at ILM and especially Christophe Moulin, and the ImagoSeine core facility. We thank Akira Nagafuchi for his generous gift of F9 cells, David Charalampous for developing the pressure control device, Alain Richert for help on tissue culture, Rémy Fulcrand for help on wafer fabrication in clean room, Pascal Hersen for letting us use his wet lab for microfluidic device preparation.

Competing interests

The authors declare no competing or financial interests.

Author contributions

Conceptualization: S.L.T., F.G., H.D.-A.; Methodology: S.L.T., F.G., H.D.-A.; Software: S.L.T., H.D.-A.; Validation: S.L.T., F.G., H.D.-A.; Formal analysis: S.L.T., F.G., H.D.-A.; Investigation: S.L.T., H.D.-A.; Writing - original draft: S.L.T., F.G., H.D.-A.; Visualization: S.L.T.; Funding acquisition: F.G., H.D.-A.

Funding

This work was funded by the Domaine d'Intérêt Majeur Logiciels et Systèmes Complexes (Région Ile de France).

Peer review history

The peer review history is available online at https://journals.biologists.com/dev/lookup/doi/10.1242/dev.200774.reviewer-comments.pdf.

References

Bardet, P., Guirao, B., Paoletti, C., Serman, F., Léopold, V., Bosveld, F., Goya, Y., Mirouse, V., Graner, F. and Bellaïche, Y. (2013). PTEN controls junction lengthening and stability during cell rearrangement in epithelial tissue. *Dev. Cell* **5**, 534-546. doi:10.1016/j.devcel.2013.04.020

Bi, D., Lopez, J. H., Schwarz, J. M. and Manning, M. L. (2014). Energy barriers govern glassy dynamics in tissues. *Soft Mat.* **10**, 1885-1890. doi:10.1039/c3sm52893f

Brodland, G. W., Conte, V., Cranston, P. G., Veldhuis, J., Narasimhan, S., Hutson, M. S., Jacinto, A., Ulrich, F., Baum, B. and Miodownik, M. (2010). Video force microscopy reveals the mechanics of ventral furrow invagination in Drosophila. *Proc. Natl. Acad. Sci. USA* **107**, 22111-22116. doi:10.1073/pnas.1006591107

Brückner, D., Fink, A., Schreiber, C., Röttgermann, P., Rädler, J. and Broedersz, C. (2019). Stochastic nonlinear dynamics of confined cell migration in two-state systems. *Nat. Phys.* **15**, 595-601. doi:10.1038/s41567-019-0445-4

Campàs, O., Mammoto, T., Hasso, S., Sperling, R. A., O'Connell, D., Bischof, A. G., Maas, R., Weitz, D. A., Mahadevan, L. and Ingber, D. E. (2014). Quantifying cell-generated mechanical forces within living embryonic tissues. *Nat. Methods* **11**, 183-189. doi:10.1038/nmeth.2761

Cantat, I., Cohen-Addad, S., Elias, F., Graner, F., Höhler, R., Pitois, O., Rouyer, F. and Saint-Jalmes, A. (2013). *Foams: Structure And Dynamics* (ed. S. J. Cox). Oxford University Press.

Cheddadi, I., Saramito, P., Dollet, B., Raufaste, C. and Graner, F. (2011). Understanding and predicting viscous, elastic, plastic flows. *Eur. Phys. J. E* **34**, 1-15. doi:10.1140/epje/i2011-11001-4

David, R., Luu, O., Damm, E. W., Wen, J. W. H., Nagel, M. and Winklbauer, R. (2014). Tissue cohesion and the mechanics of cell rearrangement. *Development* **141**, 3672-3682. doi:10.1242/dev.104315

Dolega, M. E., Delarue, M., Ingremeau, F., Prost, J., Delon, A. and Cappello, G. (2017). Cell-like pressure sensors reveal increase of mechanical stress towards the core of multicellular spheroids under compression. *Nat. Commun.* **8**, 14056. doi:10.1038/ncomms14056

Du, V., Luciani, N., Richard, S., Mary, G., Gay, C., Mazuel, F., Reffay, M., Menasché, P., Agbulut, O. and Wilhelm, C. (2017). A 3D magnetic tissue stretcher for remote mechanical control of embryonic stem cell differentiation. *Nat. Commun.* **8**, 400. doi:10.1038/s41467-017-00543-2

Durande, M., Tlili, S., Homan, T., Guirao, B., Graner, F. and Delanoë-Ayari, H. (2019). Fast determination of coarse-grained cell anisotropy and size in epithelial tissue images using Fourier transform. *Phys. Rev. E* **99**, 062401. doi:10.1103/PhysRevE.99.062401

Etournay, R., Popović, M., Merkel, M., Nandi, A., Blasse, C., Aigouy, B., Brandl, H., Myers, G., Salbreux, G., Jülicher, F. et al. (2015). Interplay of cell dynamics and epithelial tension during morphogenesis of the Drosophila pupal wing. *eLife* **4**, e07090. doi:10.7554/eLife.07090

Fernández, P., Heymann, L., Ott, A., Aksel, N. and Pullarkat, P. A. (2007). Shear rheology of a cell monolayer. *New J. Phys.* **9**, 419. doi:10.1088/1367-2630/9/11/419

Fouchard, J., Wyatt, T. P. J., Proag, A., Lisica, A., Khalilgharibi, N., Recho, P., Suzanne, M., Kabla, A. and Charras, G. (2020). Curling of epithelial monolayers reveals coupling between active bending and tissue tension. *Proc. Natl Acad. Sci. USA* **117**, 9377-9383. doi:10.1073/pnas.1917838117

Golovkova, I., Montel, L., Wandersman, E., Bertrand, T., Prevost, A. M. and Pontani, L.-L. (2020). Depletion attraction impairs the plasticity of emulsions flowing in a constriction. *Soft Mat.* **16**, 3294-3302. doi:10.1039/C9SM02343G

Graner, F., Dollet, B., Raufaste, C. and Marmottant, P. (2008). Discrete rearranging disordered patterns, part I: robust statistical tools in two or three dimensions. *Eur. Phys. J. E* **25**, 349-369. doi:10.1140/epje/i2007-10298-8

Grosser, S., Lippoldt, J., Oswald, L., Merkel, M., Sussman, D. M., Renner, F., Gottheil, P., Morawetz, E. W., Fuhs, T., Xie, X. et al. (2021). Cell and nucleus shape as an indicator of tissue fluidity in carcinoma. *Phys. Rev. X* **11**, 011033. doi:10.1103/PhysRevX.11.011033

Guevorkian, K., Colbert, M.-J., Durth, M., Dufour, S. and Brochard-Wyart, F. (2010). Aspiration of biological viscoelastic drops. *Phys. Rev. Lett.* **104**, 1-4. doi:10.1103/PhysRevLett.104.218101

Guirao, B. and Bellaïche, Y. (2017). Biomechanics of cell rearrangements in Drosophila. *Curr. Opin. Cell Biol.* **48**, 113-124. doi:10.1016/j.ceb.2017.06.004

Guirao, B., Rigaud, S. U., Bosveld, F., Bailles, A., López-Gay, J., Ishihara, S., Sugimura, K., Graner, F. and Bellaïche, Y. (2015). Unified quantitative characterization of epithelial tissue development. *eLife* **4**, e08519. doi:10.7554/eLife.08519

Harris, A. R., Peter, L., Bellis, J., Baum, B., Kabla, A. J. and Charras, G. T. (2012). Characterizing the mechanics of cultured cell monolayers. *Proc. Natl. Acad. Sci. USA* **109**, 16449-16454. doi:10.1073/pnas.1213301109

Hashmi, A., Tlili, S., Perrin, P., Lowndes, M., Peradziryi, H., Brickman, J. M., Martínez Arias, A. and Lenne, P.-F. (2022). Cell-state transitions and collective cell movement generate an endoderm-like region in gastruloids. *eLife* **11**, e59371. doi:10.7554/eLife.59371

Heisenberg, C.-P. and Bellaïche, Y. (2013). Forces in tissue morphogenesis and patterning. *Cell* **153**, 948-962. doi:10.1016/j.cell.2013.05.008
Hopkins, A., Chiang, M., Loewe, B., Marenduzzo, D. and Marchetti, C. (2022). Yield stress and compliance in active cell monolayers. *Phys. Rev. Lett.* **129**, 148101. doi:10.1103/PhysRevLett.129.148101
Iyer, K. V., Piscitello-Gómez, R., Paijmans, J., Jülicher, F. and Eaton, S. (2019). Epithelial viscoelasticity is regulated by mechanosensitive E-cadherin turnover. *Curr. Biol.* **29**, 578-591.e5. doi:10.1016/j.cub.2019.01.021
Khalilgharibi, N., Fouchard, J., Recho, P., Charras, G. and Kabla, A. (2016). The dynamic mechanical properties of cellularised aggregates. *Curr. Opin. Cell Biol* **42**, 113-120. doi:10.1016/j.ceb.2016.06.003
Lucas, B. D. and Kanade, T. (1981). Proceedings DARPA Image Understanding Workshop, April 1981, pp. 121-130. In Proc. 7th Intl Joint Conf on Artificial Intelligence (LICAL).
Marmottant, P., Mgharbel, A., Käfer, J., Audren, B., Rieu, J.-P., Vial, J., van der Sanden, B., Marée, A., Graner, F. and Delanoë-Ayari, H. (2009). The role of fluctuations and stress on the effective viscosity of cell aggregates. *Proc. Natl. Acad. Sci. USA* **106**, 17271. doi:10.1073/pnas.0902085106
Mary, G., Mazuel, F., Nier, V., Fage, F., Nagle, I., Devaud, L., Bacri, J.-C., Asnacios, S., Asnacios, A., Gay, C. et al. (2022). All-in-one rheology of multicellular aggregates. *Phys. Rev. E* **105**, 054407. doi:10.1103/PhysRevE.105.054407
Mombach, J. C. M., Robert, D., Graner, F., Gillet, G., Thomas, G. L., Idiart, M. and Rieu, J.-P. (2005). Rounding of aggregates of biological cells: Experiments and simulations. *Physica A* **352**, 525-534. doi:10.1016/j.physa.2005.02.008
Mongera, A., Rowghanian, P., Gustafson, H. J., Shelton, E., Kealhofer, D. A., Carn, E. K., Serwane, F., Lucio, A. A., Giammona, J. and Campàs, O. (2018). A fluid-to-solid jamming transition underlies vertebrate body axis elongation. *Nature* **561**, 401-405. doi:10.1038/s41586-018-0479-2
Montel, F., Delarue, M., Elgeti, J., Vignjevic, D., Cappello, G. and Prost, J. (2012). Isotropic stress reduces cell proliferation in tumor spheroids. *New J. Phys.* **14**, 055008. doi:10.1088/1367-2630/14/5/055008
Nagafuchi, A., Shirayoshi, Y., Okazaki, K., Yasuda, K. and Takeichi, M. (1987). Transformation of cell adhesion properties by exogenously introduced E-cadherin cDNA. *Nature* **329**, 341-343. doi:10.1038/329341a0
Nishizawa, K., Lin, S.-Z., Chardès, C., Rupprecht, J.-F. and Lenne, P.-F. (2022). Two-point optical manipulation reveals mechanosensitive remodeling of cell-cell contacts in vivo. *bioRxiv* 2022.07.08.499278.
Perez, J. E., Fage, F., Pereira, D., Abou-Hassan, A., Asnacios, S., Asnacios, A. and Wilhelm, C. (2021). Transient cell stiffening triggered by magnetic nanoparticle exposure. *J. Nanobiotechnol.* **19**, 117. doi:10.1186/s12951-021-00790-y
Rauzi, M., Verant, P., Lecuit, T. and Lenne, P.-F. (2008). Nature and anisotropy of cortical forces orienting Drosophila tissue morphogenesis. *Nat. Cell Biol.* **10**, 1401-1410. doi:10.1038/ncb1798
Regev, I., Guevorkian, K., Pourquie, O. and Mahadevan, L. (2022). Rectified random cell motility as a mechanism for embryo elongation. *Development* **149**, 199423. doi:10.1242/dev.199423
Roffay, C., Chan, C. J., Guirao, B., Hiiragi, T. and Graner, F. (2021). Inferring cell junction tension and pressure from cell geometry. *Development* **148**, dev.192773. doi:10.1242/dev.192773
Souchaud, A., Boutillon, A., Charron, G., Asnacios, A., Noûs, C., David, N. B., Graner, F. and Gallet, F. (2022). Live 3D imaging and mapping of shear stresses within tissues using incompressible elastic beads. *Development* **149**, 199765. doi:10.1242/dev.199765
Stirbat, T. V. (2013). Microscopic origin of the rheological and surface properties of embryonic cell aggregates. *PhD thesis*, Université Lyon 1, France.
Stirbat, T. V., Mgharbel, A., Bodennec, S., Ferri, K., Mertani, H. C., Rieu, J.-P. and Delanoë-Ayari, H. (2013). Fine tuning of tissues viscosity and surface tension through contractility suggests a new role for α-Catenin. *PLoS One* **8**, e52554. doi:10.1371/journal.pone.0052554
Takebe, T. and Wells, J. M. (2019). Organoids by design. *Science* **364**, 956-959. doi:10.1126/science.aaw7567
Tlili, S., Gay, C., Graner, F., Marcq, P., Molino, F. and Saramito, P. (2015). Colloquium: Mechanical formalisms for tissue dynamics. *Eur. Phys. J. E* **38**, 33. doi:10.1140/epje/i2015-15033-4
Tlili, S., Durande, M., Gay, C., Ladoux, B., Graner, F. and Delanoë-Ayari, H. (2020). Migrating epithelial monolayer flows like a Maxwell viscoelastic liquid. *Phys. Rev. Lett.* **125**, 88102. doi:10.1103/PhysRevLett.125.088102
Wyatt, T. P. J., Harris, A. R., Lam, M., Cheng, Q., Bellis, J., Dimitracopoulos, A., Kabla, A. J., Charras, G. T. and Baum, B. (2015). Emergence of homeostatic epithelial packing and stress dissipation through divisions oriented along the long cell axis. *Proc. Natl. Acad. Sci. USA* **112**, 5726-5731. doi:10.1073/pnas.1420585112
Yousafzai, M. S., Yadav, V., Amiri, S., Staddon, M., Tabatabai, A. P., Errami, Y., Jaspard, G., Amiri, S., Banerjee, S. and Murrell, M. P. (2020). Tissue pressure and cell traction compensate to drive robust aggregate spreading. *bioRxiv* 2020.08.29.273334.

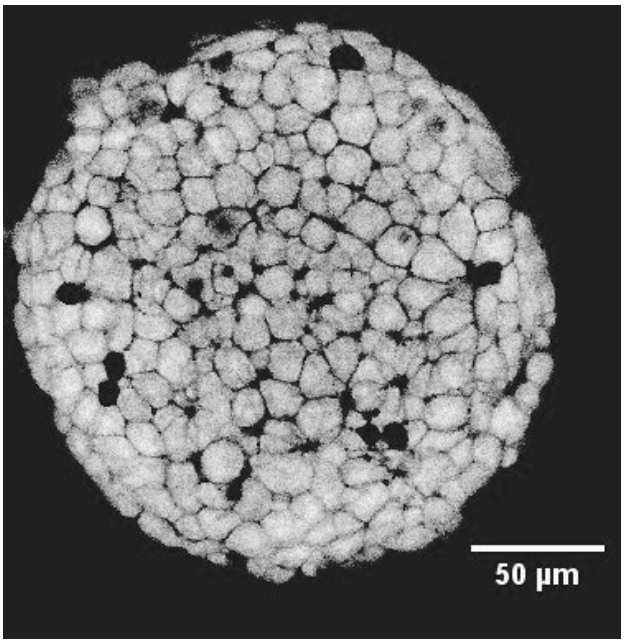

Fig. S1. F9 cell aggregate mid-section (two-photon microscopy).

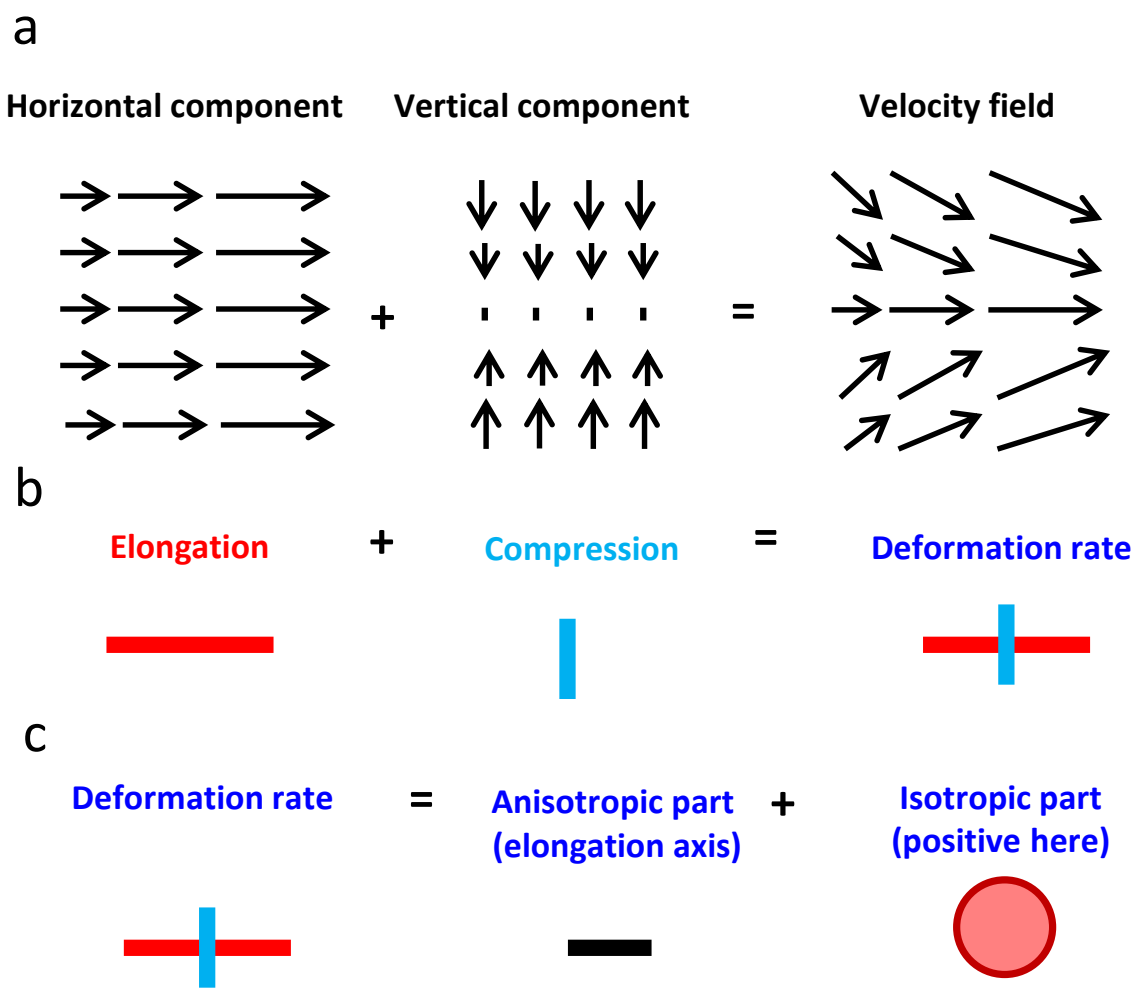

Fig. S2. (a) Decomposition in horizontal and vertical components of a typical velocity field in the constriction. (b) Corresponding graphical representation of deformation rate (15). (c) Decomposition of the deformation rate in anisotropic and isotropic parts, and corresponding graphical representation (15).

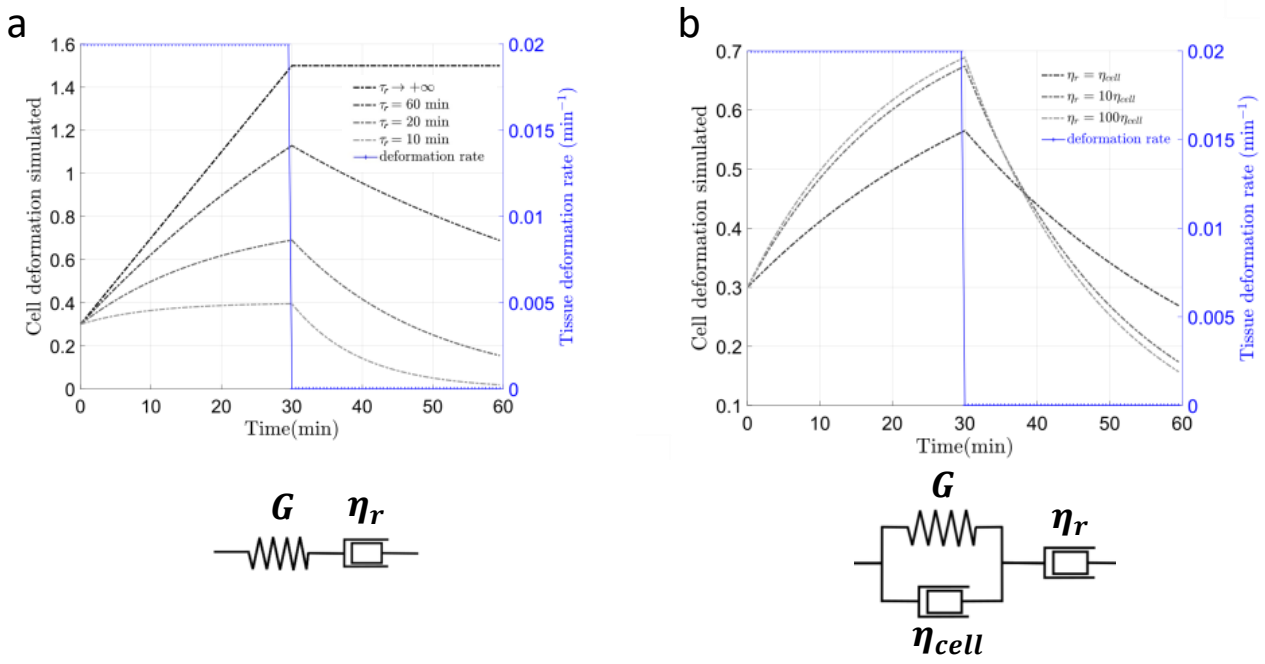

Fig. S3. Idealized mechanical responses. Simulated time evolutions for different models (insets in a,b), τ_r values and viscosity ratios of the response to an imposed deformation rate step. Simulated equations are for (a) $\dot{\varepsilon}^{\mathrm{dev}}_{cell} = (\mathrm{grad}\,\vec{v})^{\mathrm{dev}}_{\mathrm{sym}} - \frac{\varepsilon^{\mathrm{dev}}_{cell}}{\tau_r}$ and for (b) $(1+\frac{\eta_{cell}}{\eta_r})\dot{\varepsilon}^{\mathrm{dev}}_{cell} = (\mathrm{grad}\,\vec{v})^{\mathrm{dev}}_{\mathrm{sym}} - \frac{\varepsilon^{\mathrm{dev}}_{cell}}{\tau_r}$.

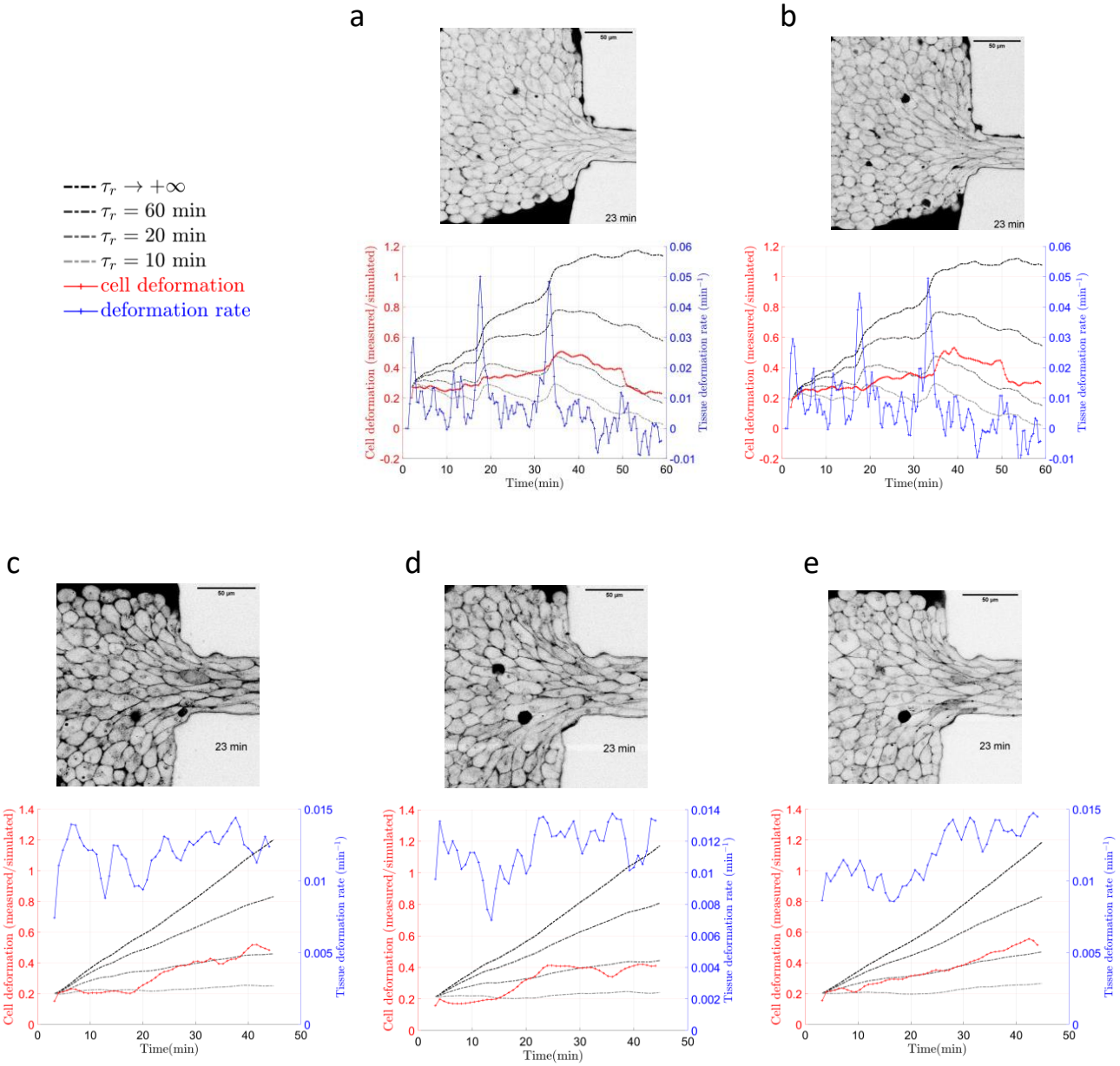

Fig. S4. Reproducibility in estimating τ_r (same analysis and imaging methods as in Fig. 4). (a,b) Same experiment as in Fig. 4, imaged and analyzed at two different heights (Supp. Movie 14); (a) is Fig. 4c duplicated here to enable comparison taken at z = 15 μm from the coverslip and (b) at z = 30 μm from the coverslip. (c-e) Another experiment, imaged and analyzed at three different heights (Supp. Movie 15) (Heights: (c) z = 20 μm, (d) z = 30 μm and (e) z = 40 μm from the coverslip).

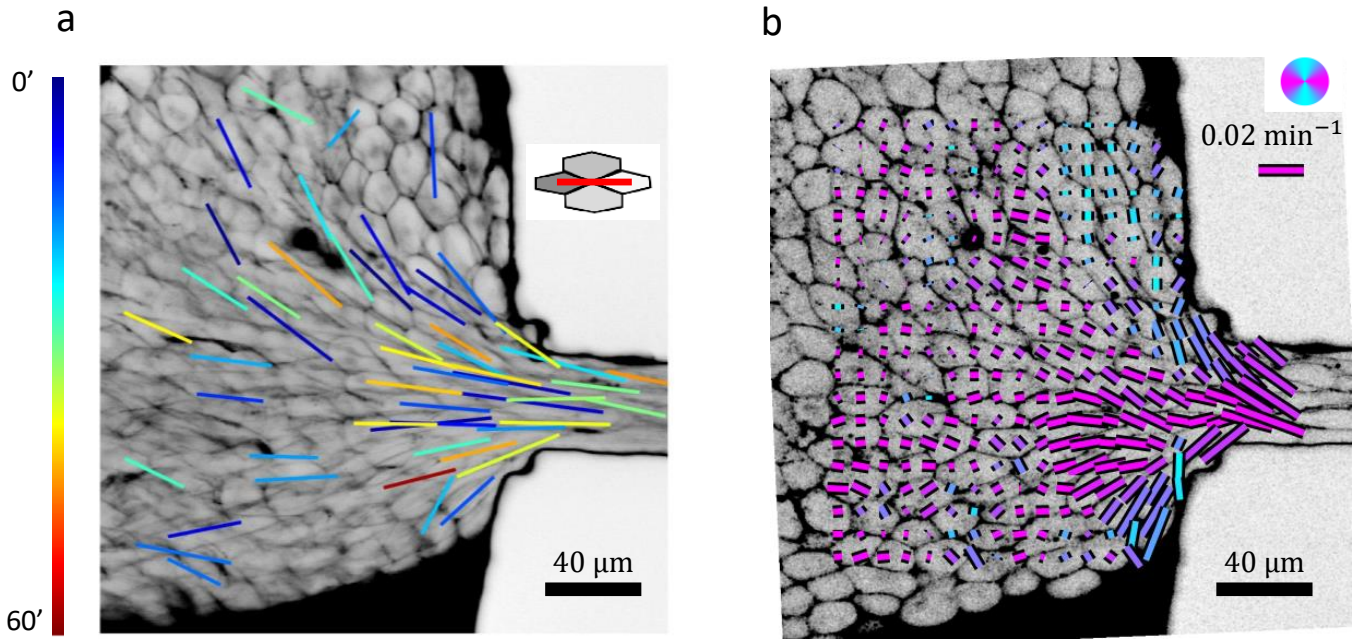

Fig. S5. Cell rearrangement map. Rearrangements are detected in Supp. Movie 4 during one hour. (a) Position and orientation of the rearrangements detected, plotted as a bar linking both centers of cells that will lose contact just before the rearrangement (inset), and color-coded according to the timing of the four-vertex stage (in minutes). (b) Deformation rate anisotropic part averaged over time (60 minutes) with the bars color coding for their angle with respect to the channel. Zones of high rearrangements frequency correspond to high deformation rate zones.

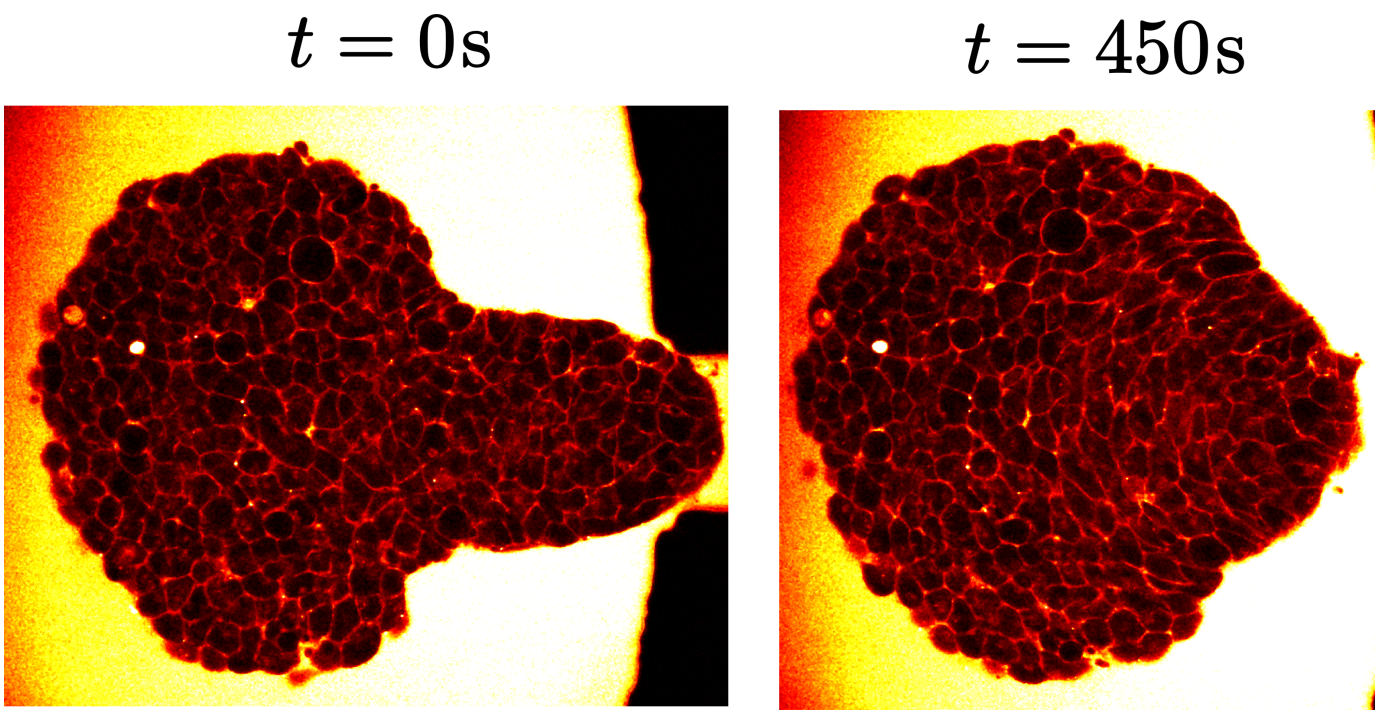

Fig. S6. Aggregate compaction after a relaxation. An aggregate has been aspired during 1000 s. It is pushed back in the reservoir and cell shapes relax within a few seconds. Time t = 0 corresponds to 20 s after the pushing and cell shapes have already almost totally relaxed. After 450 s, the aggregate as a whole is round, but not each cell individually (Supp. Movie 9).

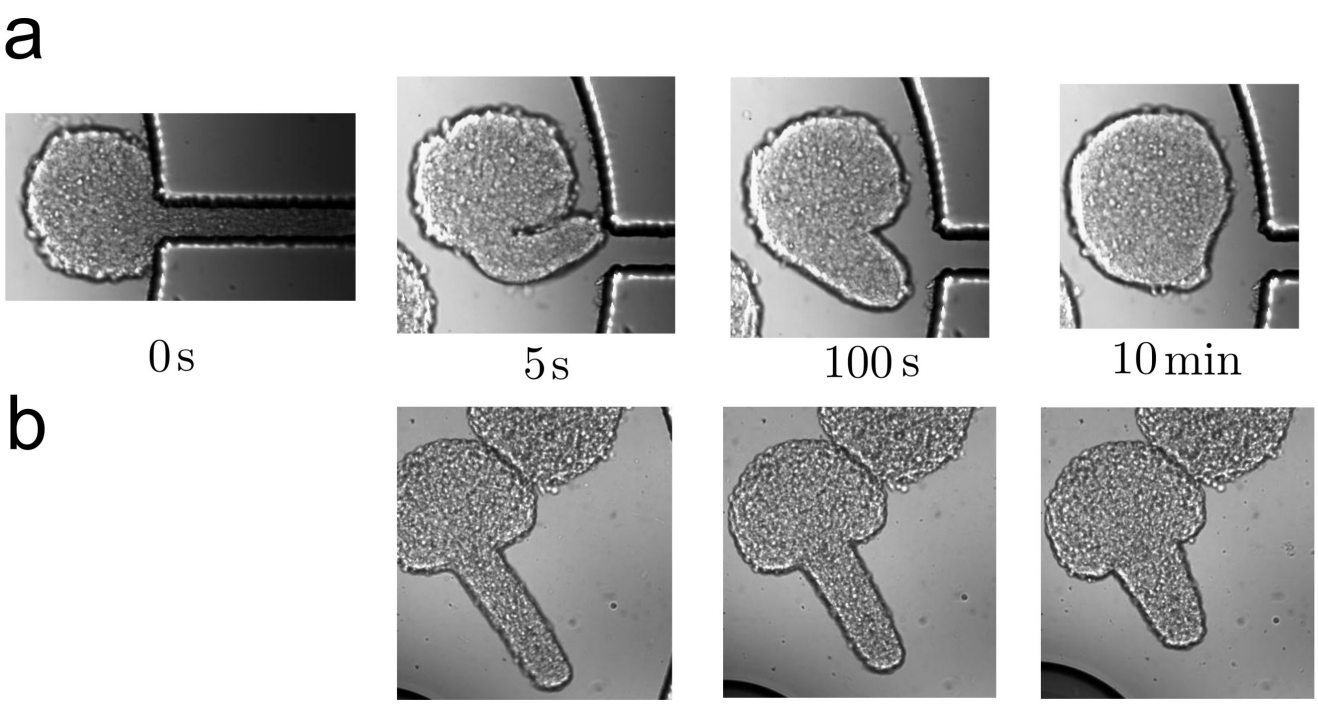

Fig. S7. First and second phases of relaxation. (a) Brightfield image of aggregate relaxation. After a 1000 seconds long aspiration, the aggregate is left free to relax. Time t = 0 is counted at the end of the aspiration, *i.e.* at the beginning of the relaxation. (b) Same with 50 µM of blebbistatin to inhibit myosin II. The first fast phase of the relaxation is still present, but there is no complete return to the initial shape.

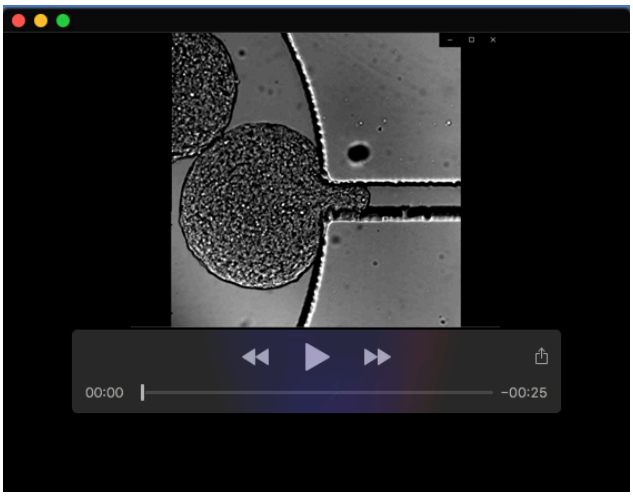

Movie 1. 40 minutes long timelapse (brightfield) of an aggregate aspired in a channel.

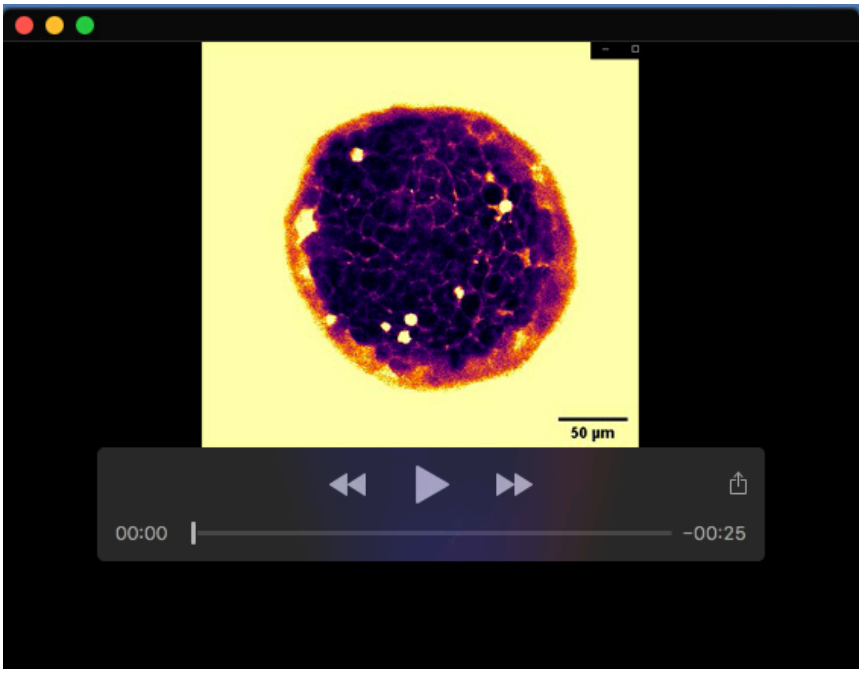

Movie 2. *z*-stack (two-photon microscopy) of a non-deformed F9 cells aggregate.

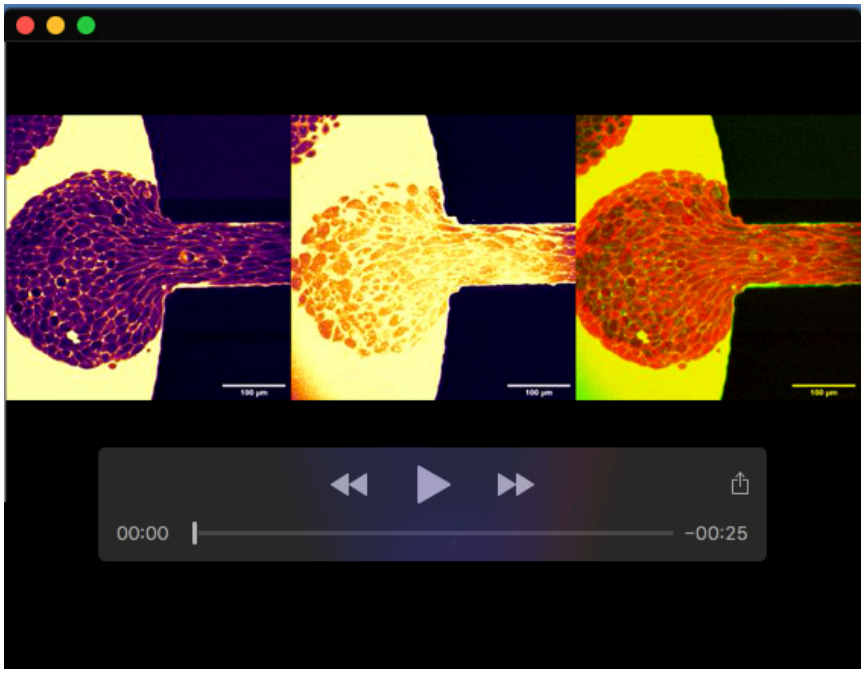

Movie 3. 60 minutes long timelapse (two-photon microscopy) of an aggregate aspired in a channel. Left: imaged plane at z = 40 μm from the coverslip. Middle: imaged plane in contact with the coverslip. Right: superposition of the two imaged planes.

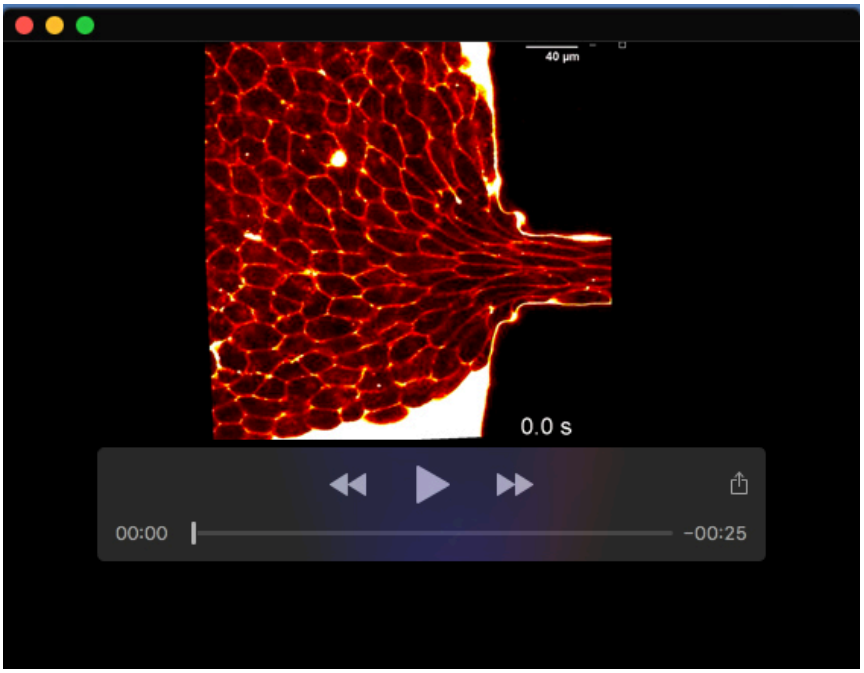

Movie 4. 60 minutes long timelapse (two-photon microscopy) of an aggregate aspired in a channel.

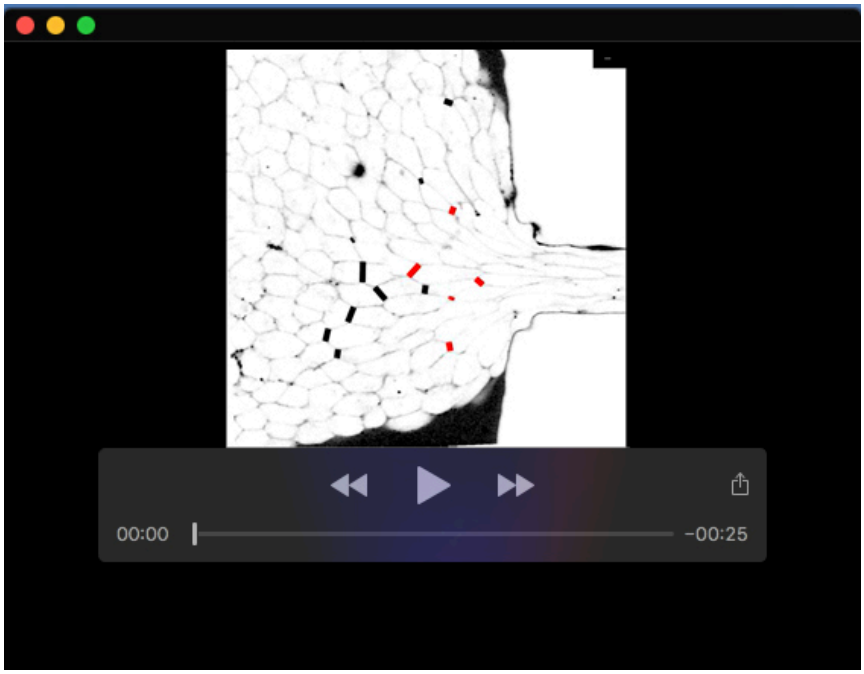

Movie 5. cell-cell junctions involved in cell rearrangements in Supplementary Movie 4. Rapid relaxation rearrangements ($V^+ > 1$ μm/min) are represented in red while slow ones ($V^+ < 1$ μm/min) are in black.

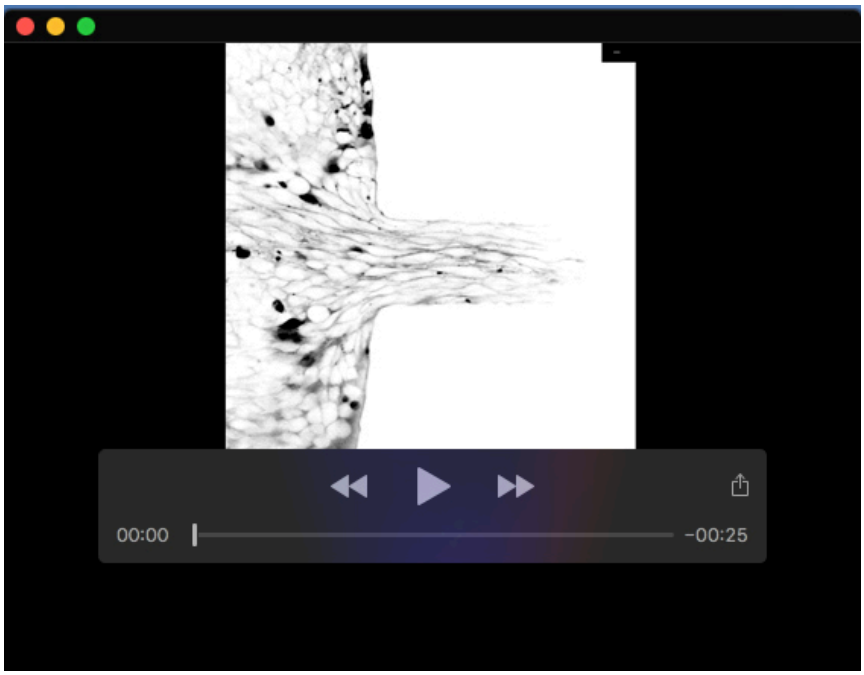

Movie 6. tissue fracture appearing during a rapid aspiration (two-photon microscopy timelapse).

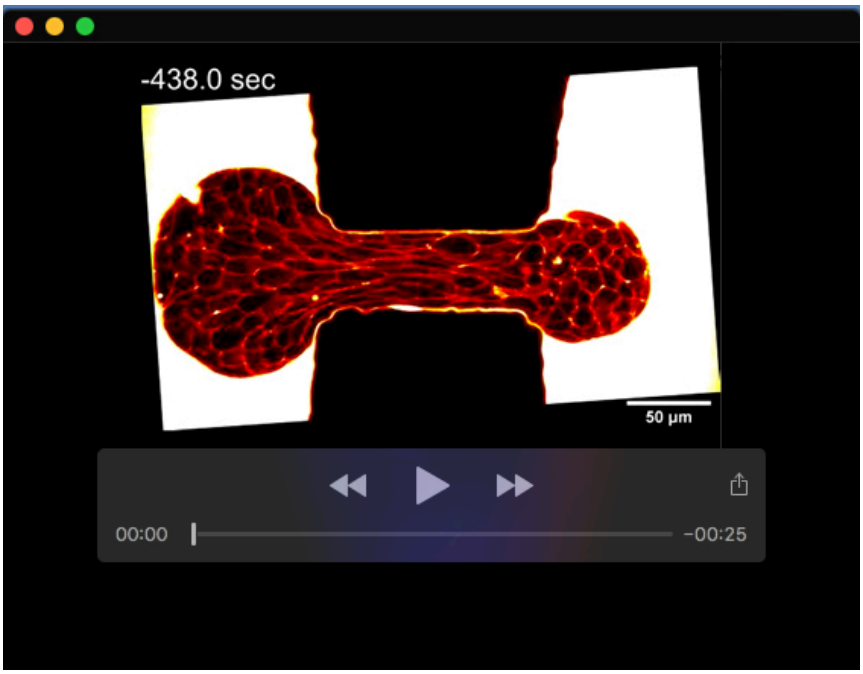

Movie 7. aspiration and rapid relaxation experiment (two-photon microscopy).

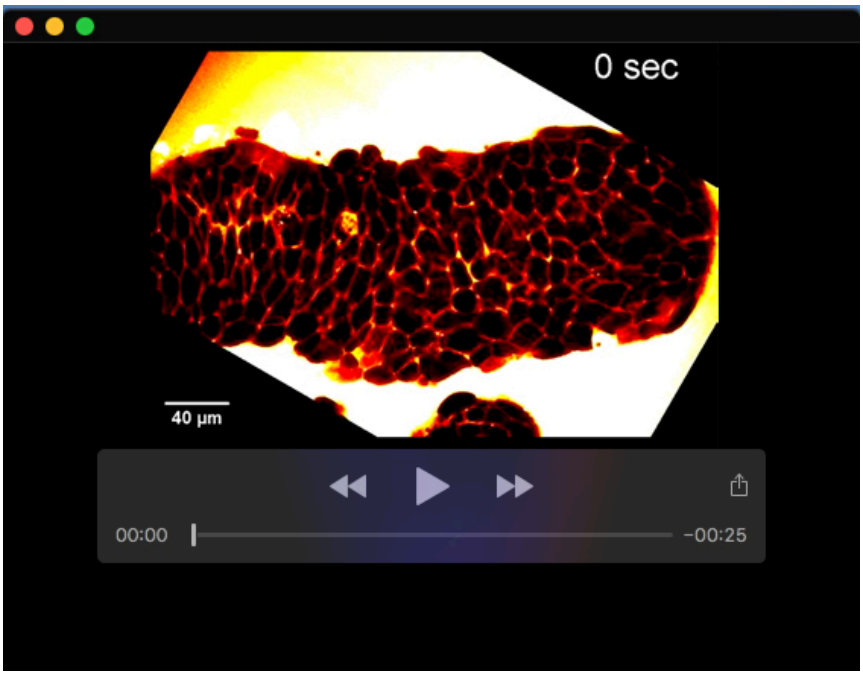

Movie 8. relaxation experiment after an aggregate being fully blocked in the aspiration channel during 30 minutes (two-photon microscopy).

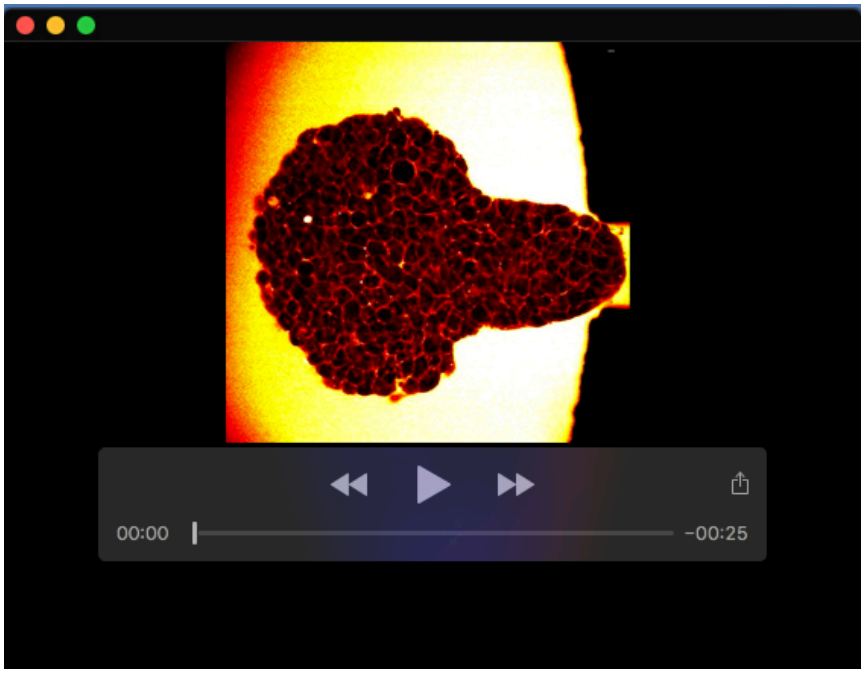

Movie 9. relaxation experiment after a partial aspiration during which cellular deformation has relaxed (two-photon microscopy).

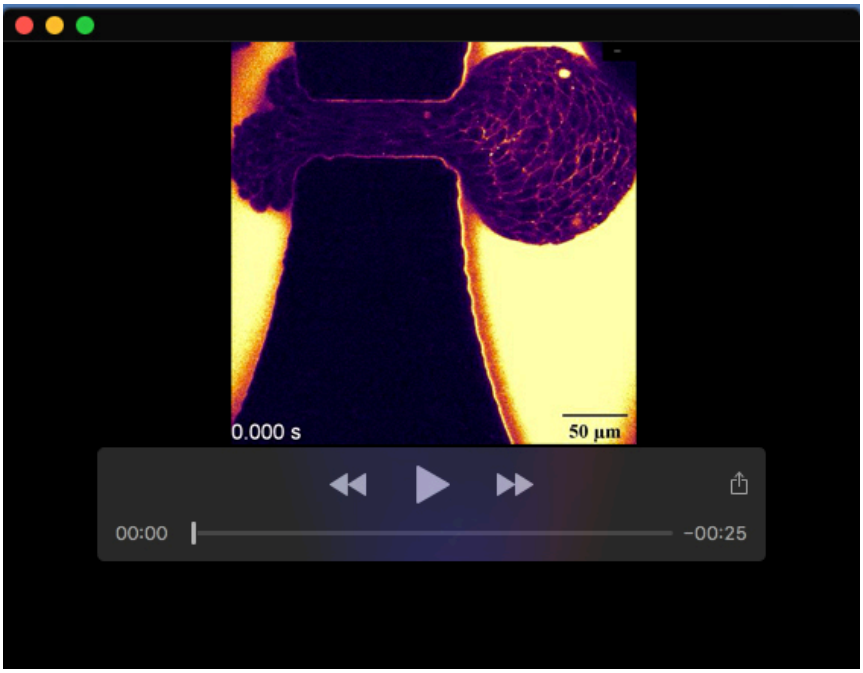

Movie 10. relaxation experiment after an aspiration in a short channel, with a more complex geometry during the rounding phase (two-photon microscopy).

Movie 11. other example of a relaxation experiment after an aspiration in a short channel (two-photon microscopy).

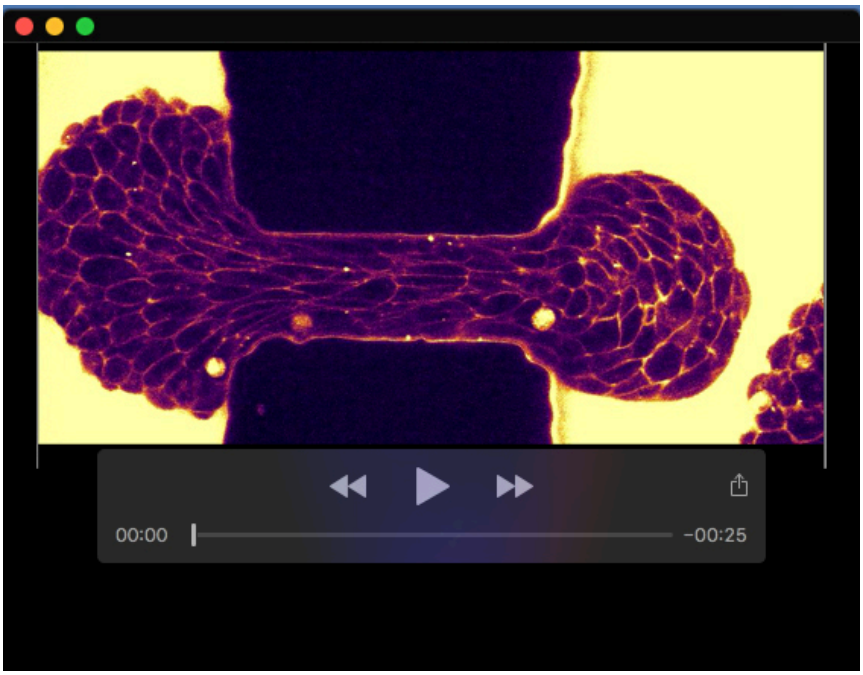

Movie 12. relaxation experiment after a partial aspiration (two-photon microscopy) in 50 μM blebbistatin medium.

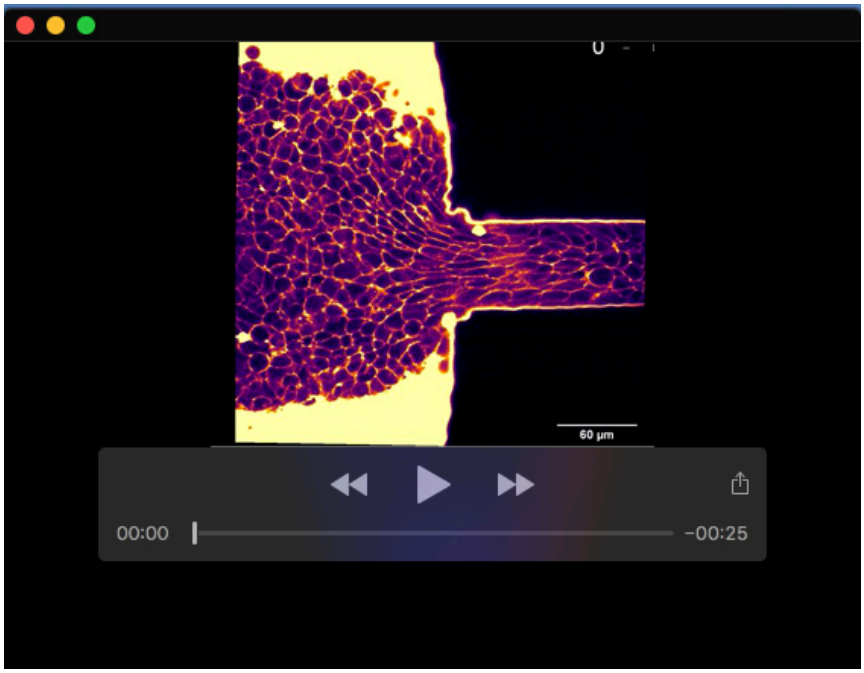

Movie 13. aspiration of an *α*-catenin null cell line aggregate (two-photon microscopy).

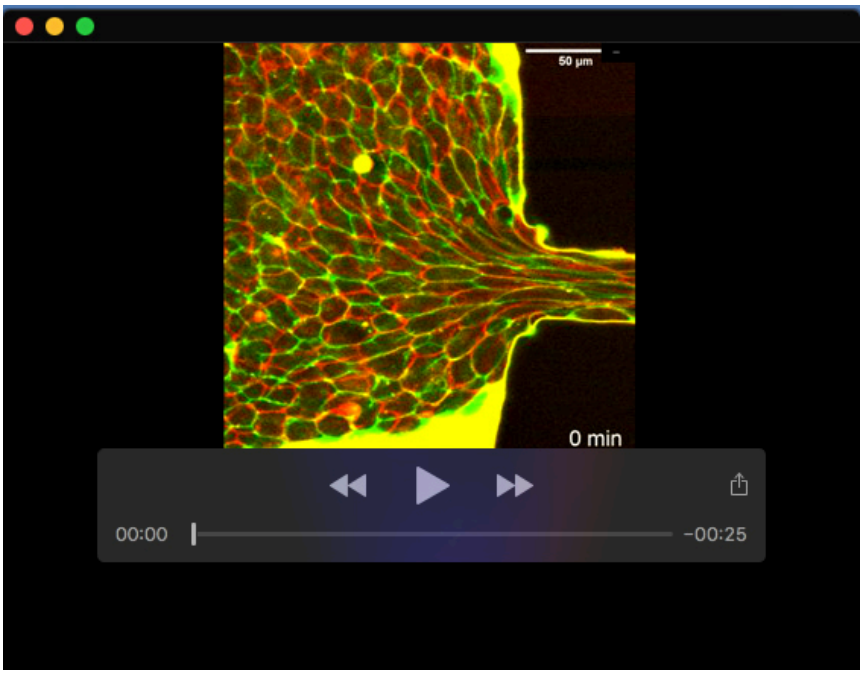

Movie 14. same aspiration as in Supp. Movie 4, with two planes superimposed in red and green (heights: z = 15 and 30 μm from the coverslip).

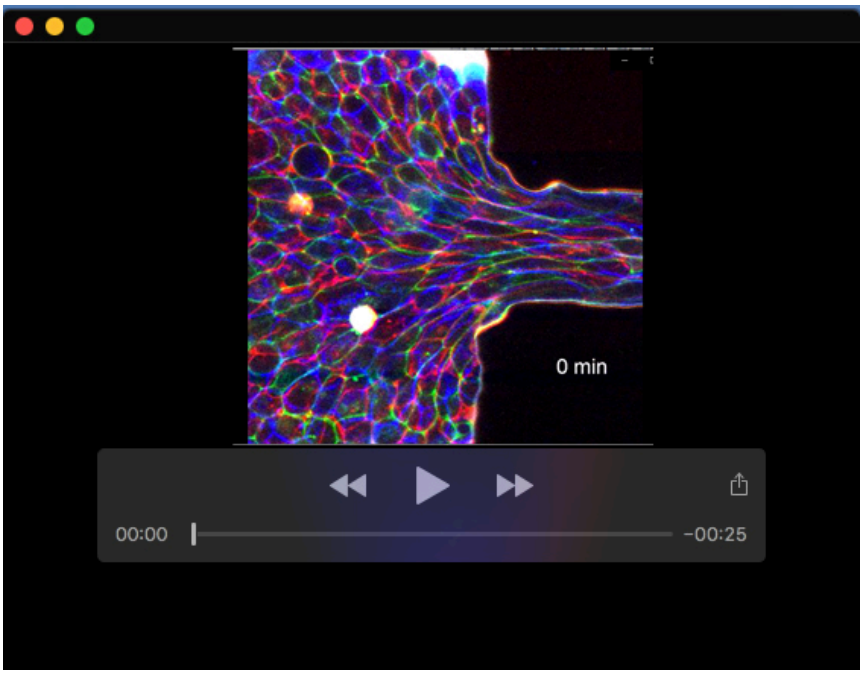

Movie 15. aspiration with three planes superimposed in red, blue and green (heights: z = 20, 30 and 40 μm from the coverslip).